Fakultät Mathematik und Naturwissenschaften
der Technischen Universität Dresden

Phase-separated manganites

The effect of reversible elastic lattice strain on the electronic properties

Dissertation
zur Erlangung des akademischen Grades
Doctor rerum naturalium
(Dr. rer. nat.)

vorgelegt von
Martina Cornelia Dekker
geboren am 1. Dezember 1982 in 's Gravenhage, Die Niederlande

Dresden
2010

Die vorliegende Dissertationsschrift wurde angefertigt am Institut für Metallische Werkstoffe des IFW Dresden.

1. Gutachter: Prof. Dr. L. Schultz
2. Gutachter: Prof. Dr. C. Jooß

Eingereicht am: 26.01.2010
Tag der Verteidigung: 15.06.2010

For my parents

Abstract

In this work, the effect of reversible elastic lattice strain on the electronic properties of a) $(Pr_{1-y}La_y)_{0.7}Ca_{0.3}MnO_3$ (PLCMO) thin films and b) the interface layer of $La_{0.7}Sr_{0.3}MnO_3$ (LSMO) with $SrTiO_3$ (STO) has been determined using piezoelectric substrates. Lattice strain is known to effectively alter the electronic structure of compounds from the manganite family, since it shifts the balance of competing electronic interactions by changing bond angles and bond lengths.

The PLCMO films have been prepared by pulsed laser deposition (PLD) from a $La_{0.7}Ca_{0.3}MnO_3$ (LCMO) and a $Pr_{0.7}Ca_{0.3}MnO_3$ (PCMO) target. The metal-insulator phase boundary has been established to lie around $y = 0.6$. In films with $y = 0.6$, the piezoelectric release of tensile strain in the film plane induces a drastic reduction of the resistance, or a "colossal" elastoresistance. Resistive gauge factors as high as $\Gamma = 1000$ have been found. Consistent with the transport results, the release of tensile strain leads to an increase in both the Curie temperature and the magnetisation. The coexistence of the ferromagnetic metallic (FMM) and charge ordered insulating (COI) phases in PLCMO has been found to be strongly affected by the reversible substrate strain. Both the magnetisation and the resistance data in controlled strain states demonstrate a strong suppression of the ferromagnetic double exchange interaction by tensile strain.

$[La_{0.7}Sr_{0.3}MnO/SrTiO_3]$ superlattices have been deposited on STO and piezoelectric PMN-PT (001) $(PbMg_{1/3}Nb_{2/3}O_3)_{0.72}(PbTiO_3)_{0.28}$ substrates by PLD. X-ray reflectivity (XRR) measurements show clear Kiessig fringes as well as the larger interference maxima caused by the superlattice, giving qualitative proof of a well defined superlattice structure with sharp interfaces on both substrates. With decreasing LSMO layer thickness d, the samples show a sharp decrease of the Curie temperature, accompanied by a decrease of the saturation magnetisation and an increase of the coercive field around $d = 5$ nm. Reversible strain measurements on thicker superlattices ($d = 16.7$ nm) reveal a behaviour of the magnetisation similar to that of single thick films of LSMO. When d is decreased, the strain induced relative change in magnetisation $\Delta M/M_0$ shows a behaviour comparable to PLCMO thin films. This has been attributed to the increased volume fraction of the LSMO interface layer with STO, which displays a reduced magnetic order and phase-separated tendencies. From the absolute change in magnetisation per interface, the thickness of the so-called magnetically "dead" layer of the LSMO has been estimated to lie between 13.5 Å and 17 Å in the superlattices grown on PMN-PT.

Kurzfassung

In dieser Arbeit wurden piezoelektrische Substrate verwendet, um die Abhängigkeit des elektronischen Grundzustands a) der $(Pr_{1-y}La_y)_{0.7}Ca_{0.3}MnO_3$ (PLCMO) Dünnschichten und b) der Grenzflächenschicht von $La_{0.7}Sr_{0.3}MnO_3$ (LSMO) an $SrTiO_3$ (STO) von reversiblen elastischen Gitterdehnungen zu untersuchen. Die PLCMO Dünnschichten wurden mittels gepulster Laserdeposition (PLD) abgeschieden. Die Metall-Isolator-Phasengrenze liegt bei $y \approx 0.6$. In Schichten mit $y = 0.6$ bewirkt die piezoelektrische Entspannung der in-plane-Gitterdehnung eine drastische Reduktion des elektrischen Widerstands, auch "Kolossaler" Elastowiderstand genannt. Er weist eine Dehnungsempfindlichkeit (gauge factor) Γ bis zu 1000 auf. Passend zu den Transportresultaten bewirkt die Entspannung der Gitterdehnung einen Anstieg der Curie Temperatur und eine Erhöhung der Magnetisierung. Die Koexistenz der ferromagnetisch-metallischen Phase und der ladungsgeordneten isolierenden Phase wird stark beeinflusst von den reversiblen elastischen Gitterdehnungen. Sowohl die Magnetisierungsergebnisse als auch die Widerstandsdaten zeigen eine starke Unterdrückung der ferromagnetischen Doppelaustausch-Wechselwirkung durch die Zugdehnung des Gitters.

$[La_{0.7}Sr_{0.3}MnO/SrTiO_3]$ Übergitter wurden mittels PLD auf STO und piezoelektrische PMN-PT (001) $(PbMg_{1/3}Nb_{2/3}O_3)_{0.72}(PbTiO_3)_{0.28}$ Substraten abgeschieden. Röntgenreflektivitätsmessungen (XRR) zeigen auf beiden Substraten zusätzlich zu den grösseren Interferenzmaxima der Übergitter deutliche Kiessig-Oszillationen, die einen qualitativen Beweis für gut definierte Übergitter mit scharfen Grenzflächen darstellen. Für LSMO-Schichtdicken $d < 5$ nm zeigen die Übergitter bei Verkleinerung von d eine starke Abnahme von T_C, begleitet von einer Abnahme der Sättigungsmagnetisierung und einer Zunahme des Koerzitivfeldes. Die Eigenschaften der Magnetisierung von Übergittern mit unterschiedlicher LSMO-Dicke wurden in Abhängigkeit von der Gitterdehnung untersucht. Übergitter mit $d = 16.7$ nm zeigen ein dehnungsabhängiges Magnetisierungsverhalten ähnlich einzelner LSMO Schichten auf PMN-PT. Für kleinere d-Werte verhält sich die Magnetisierung wie bei Einzelschichten von PLCMO. Dieses Verhalten kann zurückgeführt werden auf den erhöhten Volumenanteil der Grenzflächenschicht, die eine reduzierte magnetische Ordnung hat und eine Tendenz zur Phasenseparation zeigt. Aus der absoluten dehnungsabhängigen Magnetisierungsänderung pro Grenzfläche von LSMO mit STO auf PMN-PT Substraten wurde die Dicke der sogenannten magnetischen "dead layer" zwischen 13.5 Å und 17 Å abgeschätzt.

Contents

Chapter 1

Introduction

Manganites are best known for their colossal magnetoresistance (CMR), a change in resistance of several orders of magnitude upon the application of an external magnetic field. Since the discovery of the CMR effect in 1993 in thin film $La_{2/3}Ba_{1/3}MnO_3$ by von Helmholt *et al.* [1], many studies have been devoted to the exploration of this curious phenomenon. It has been generally accepted that the double exchange interaction introduced by Zener [2] underlies the increase in conductivity found upon the alignment of the Mn spins. Furthermore, local deformations of the O_6 octahedra, known as Jahn-Teller distortions, may trap the conduction electrons in their self-induced potential minima, causing the insulating state above T_C. It has been argued that the CMR effect is ultimately the result of a phase-separation of the electronic state of the manganites into ferromagnetic metallic and charge ordered insulating clusters [3, 4]. While in some materials, the phase-separation may be disorder driven, occurring close to a first order transition only, in others, it may result from the different hole densities of the clusters of the competing phases. The latter case, of electronically driven phase-separation, can exist on a nanometer length scale only, since the Coulomb energy of the clusters will grow with cluster size.

Manganites are strongly correlated electron systems. The kinetic energy of the electrons depends sensitively on the spin and lattice degrees of freedom, and in turn has a strong influence on their behaviour. As a result, compositional tuning reveals a myriad of possible electronic and structural phases: conductivity may be anywhere between highly conducting and insulating, and ferromagnetic phases as well as various types of charge and orbital ordered antiferromagnets have been found. In addition, dramatic variations of the physical properties may be found in dependence on parameters such as temperature, hydrostatic pressure, irradiation with light or x-rays, application of electric and magnetic DC fields, and, in thin films, epitaxial strain [5, 6].

This work describes the effect of reversible elastic lattice strain on the phase-separated electronic properties of a) $(Pr_{1-y}La_y)_{0.7}Ca_{0.3}MnO_3$ (PLCMO) thin films and b) the interface layer of thin film $La_{0.7}Sr_{0.3}MnO_3$ (LSMO) with $SrTiO_3$ (STO).

In **chapter 2** the structure and properties of the rare earth manganites are introduced. The CMR effect is addressed, as well as the phase-separated nature of PLCMO and the magnetically "dead" layer of LSMO at the interface with STO. A

model is described for the influence of epitaxial strain on the magnetisation in thin film manganites.

In **chapter 3**, the fabrication of the films by pulsed laser deposition is described. **Chapter 4** deals with the techniques used to characterise the samples.

Chapter 5 reports on the investigation of thin films of $(Pr_{1-y}La_y)_{0.7}Ca_{0.3}MnO_3$. The dependence of the magnetic and electronic ground state on the composition y is discussed. The influence of reversible substrate strain on the resistance and magnetisation of the films is described, in particular of those films that have a composition close to the metal-insulator phase boundary of the ground state.

Lastly, the properties of superlattices of $La_{0.7}Sr_{0.3}MnO_3$ and $SrTiO_3$ are described in **chapter 6**. The superlattice quality of samples grown on STO and PMN-PT substrates is compared, and the magnetic behaviour of the superlattices is discussed in dependence on the thickness of the LSMO layer. From reversible strain measurements of the magnetisation a value for the thickness of the so-called magnetically "dead" layer of the LSMO is derived.

Bibliography

[1] *Giant negative magnetoresistance in perovskitelike $La_{2/3}Ba_{1/3}MnO_x$ ferromagnetic films*, R. von Helmolt, J. Wecker, B. Holzapfel, L. Schultz, K. Samwer, Phys. Rev. Lett. **71**, 2331 (1993)

[2] *Interaction between the d-Shells in the Transition Metals. II. Ferromagnetic Compounds of Manganese with Perovskite Structure*, C. Zener, Phys. Rev. **82**, 403 (1951)

[3] *Open questions in CMR manganites, relevance of clustered states and analogies with other compounds including the cuprates*, E. Dagotto, New Journal of Phys. **7**, 67 (2005)

[4] *Recent developments in the theoretical study of phase separation in manganites and underdoped cuprates*, E. Dagotto, S. Yunoki, C. Şen, G. Alvarez, A. Moreo, J. Phys.: Condens. Matter **20**, 434224 (2008)

[5] *Ferromagnetic manganites: spin-polarized conduction versus competing interactions*, K. Dörr, J. Phys. D: Appl. Phys. **39**, 125 (2006)

[6] *Critical features of colossal magnetoresistive manganites*, Y. Tokura, Rep. Prog. Phys. **69**, 797 (2006)

Chapter 2

Doped rare earth manganites

2.1 Structure and electronic properties

Doped manganese oxides $RE_{1-x}AE_x\mathrm{MnO_3}$ (RE = rare earth metal, AE = divalent alkaline earth) are materials that crystallise in the so-called perovskite $AB\mathrm{O_3}$ structure. The original Perovskite $\mathrm{CaTiO_3}$ consists of a simple cubic lattice of Ca atoms, enclosing an oxygen octahedron with a Ti atom at its centre (figure 2.1). In the manganites, the B site is taken up by the Mn ion, while the A site can be occupied by a trivalent rare earth element, a divalent alkali earth metal, or, in the case of the doped manganites, a combination of the two.

A free manganese ion has five degenerate 3d orbitals, which can be classed by their angular distribution (figure 2.2). Two of the orbitals, d_{z^2} and $\mathrm{d}_{x^2-y^2}$, have lobes which lie along the x, y and z axis, while the other three, d_{xy}, d_{yz} and d_{zx}, point with their lobes between the axes (figure 2.2). Placed inside the perovskite structure, the $\mathrm{Mn^{3+}}$ 3d orbitals interact with the crystal field of the oxygen octahedron, forming

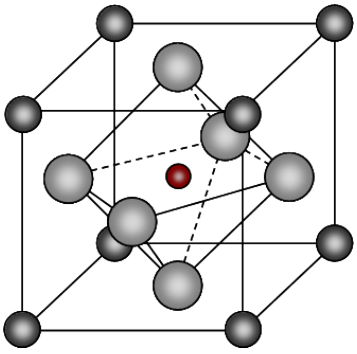

Figure 2.1: The unit cell of an $AB\mathrm{O_3}$ type perovskite consists of a B ion enclosed by an oxygen octahedron inside a simple cubic lattice of A atoms.

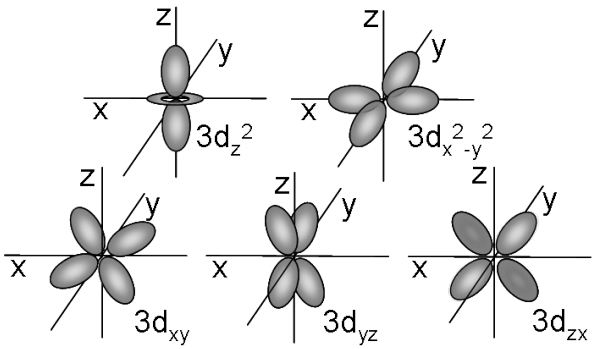

Figure 2.2: Angular distribution of the 3d electron orbitals. The e_g levels d_{z^2} and $\mathrm{d}_{x^2-y^2}$ point with their lobes along the x, y or z axis. The t_{2g} orbitals d_{xy}, d_{yz} and d_{zx} have lobes that lie between the axes.

four covalent bonds with the oxygen 2p orbitals. This interaction will partially lift the degeneracy of the electron orbitals into a high energy e_g doublet (d_{z^2} and $d_{x^2-y^2}$) and a lower energy t_{2g} triplet (d_{xy}, d_{yz} and d_{zx}) (figure 2.3). Hund's first rule states that electron spins in a p or d shell that is up to half filled align parallel in order to minimise the Coulomb repulsion energy, and the energy levels of the Mn^{3+} ion are filled accordingly. In the all-Mn^{3+}-based compound $LaMnO_3$, the 3d electrons are strongly hybridised with the oxygen 2p states and tend to localise, forming an insulating structure with an antiferromagnetic ground state.

When electron vacancies, or holes, are created in the e_g orbital states of the manganese ion (e.g. by doping with a di-valent alkali earth metal), the e_g electrons can become itinerant. The hole doping corresponds to the creation of mobile Mn^{4+} species on the manganese sites. The t_{2g} electrons, on the other hand, are less hybridised with the oxygen 2p electrons and stabilised by the crystal field splitting. Even in the metallic state, they are localised, forming an electrically inert "core spin" of $S_l = 3/2$. The spin of the localised t_{2g} electrons displays a strong ferromagnetic coupling to the electron spin of the e_g conduction electrons ($S = 1/2$). The Hund's coupling energy of $J_H S_l \approx 2 - 3$ eV [1, 2] aligns the e_g spin to the t_{2g} spin. Intersite hopping of the e_g electrons is possible. The hopping probability depends on the relative angle θ between the neighbouring spins and is proportional to $\cos(\theta/2)$ [3]. This ferromagnetic hopping interaction has been termed "double exchange" (DE) interaction by Zener [4], who considered the process as a "double" exchange of an itinerant electron from the Mn^{3+} site to a Mn^{4+} site via the O 2p state.

The double exchange mechanism forms an intuitive scenario in which the large magnetoresistance effects found in manganites near the Curie temperature, as well as the emergence of a ferromagnetic metallic ground state can be understood. In the hole doped systems, the e_g electron can hop between neighbouring sites depending on the relative configuration of the core spins. At low temperature, the ferromagnetic state ($\theta = 0$) is stabilised by maximising the kinetic energy of the itinerant electrons. For $\theta = \pi$, which corresponds to an antiferromagnetic configuration, hopping is forbidden. In other words, the transition from a disordered state to a ferromagnetic state at a certain temperature will enhance the conductivity, driving a transition from an insulating to a metallic state. Slightly above T_C, the configuration of the spins is disordered (reducing the effective hopping), but easily aligned by an external magnetic field, which increases the hopping of the e_g electrons and results in a large MR effect.

The physics of the colossal magnetoresistance effect (CMR), however, is more complex. Apart from the DE scenario, factors such as electron-lattice interaction, antiferromagnetic superexchange interaction between the local t_{2g} spins, orbital ordering as a result of the intersite exchange interaction between the e_g orbitals, or the intrasite and intersite Coulomb repulsion between the e_g electrons have to be taken into account. All these interactions may compete with the double exchange mechanism, which underlies the almost endless number of electronic phases that can be obtained by compositional tuning.

A well known example of an electron-lattice interaction in the manganites is the

so-called Jahn-Teller coupling of the e_g electrons with the position of the oxygen ions in the lattice. In the case of Mn^{3+}, it is energetically favourable to shorten or elongate some of the Mn-O bonds. The cost of the increased elastic energy is balanced by the lowering of the electronic energy due to the distortion. By shortening the Mn-O bonds along the x and y axes and elongating them along the z axis, the energy of the d_{3z^2} state is reduced (figure 2.3). Alternatively, the energy of the $d_{x^2-y^2}$ orbital can be lowered by compressing the bonds in the z direction, lengthening those in the xy plane. In this way, the deformation of the oxygen octahedron lifts the degeneracy of the 3d e_g and t_{2g} levels. In the case of all-Mn^{3+} $LaMnO_3$, the Jahn-Teller distortion is a collective effect, and a static distortion of the Mn-oxygen network is realised throughout the crystal. In doped materials, a so-called breathing mode distortion in which all 6 O bonds to the Mn^{4+} ions are changed by the same amount, has also been argued to be important [5, 6].

The local lattice distortions around the Mn^{3+} ions caused by the e_g electron produce a potential minimum which can effectively trap the carrier electron. This self trapped state of the electron is called a polaron. Above T_C, electronic conduction is due to the thermally activated motion of the polarons, so that the resistance increases when the temperature is lowered. In addition to the formation of polarons, the electron movement is hindered by the breathing mode which couples to the Mn^{4+} sites. Around the Curie temperature, the self trapping mechanism starts to compete with the electrons' tendency to band-formation in the presence of parallel core spins, unbinding the trapped carrier electrons and causing a drop in resistance.

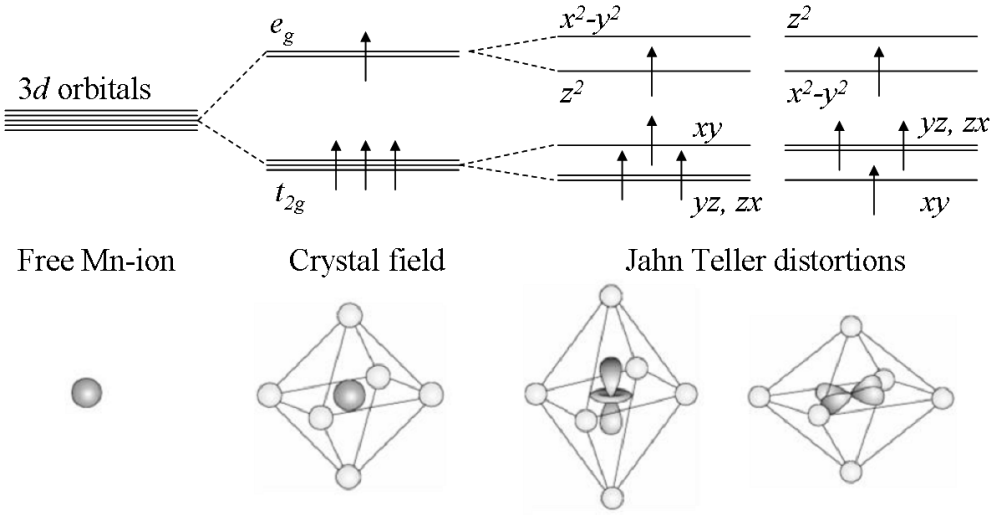

Figure 2.3: Interaction with the oxygen crystal field splits the five-fold degenerated Mn^{3+} orbitals into a higher e_g doublet and lower t_{2g} triplet state. The energetically favourable Jahn-Teller effect deforms the oxygen octahedron, further lifting the e_g and t_{2g} degeneracy.

Apart from the deformation of the MnO_6 octahedra caused by the Jahn-Teller mechanism, doping with elements with different ionic radii may cause a distortion of the perovskite ABO_3 lattice. The traditional way to characterise the perovskite crystal structure is by means of the tolerance factor t, which is a measure of the difference in ionic radius of the various crystal compounds [7, 8]. In other words, it quantifies the lattice matching between the AO and BO_2 planes:

$$t = \frac{r_A + r_O}{\sqrt{2}(r_B + r_O)}, \tag{2.1}$$

where $r_{A,B,O}$ is the mean ionic radius of the respective elements. The perovskite structure can only be stable for t close to unity, with a purely cubic structure if t equals 1, as is the case for $SrTiO_3$. As t decreases, the lattice structure will transform to rhombohedral ($0.96 < t < 1$) or orthorhombic ($t < 0.96$). In the common manganites, the tolerance factor typically varies between 1 and 0.94. The relatively small size of the A ions puts the AO bonds in the crystal under tension. As a result, the O_6 octahedra will tilt, deviating the Mn−O−Mn bond angle from 180° and decreasing the effective electron hopping, which results in a reduction of the width of the e_g conduction band. This effect is known as the "chemical pressure" effect [9].

In addition to the double exchange mechanism and the self-trapping of carrier electrons by Jahn-Teller deformations, phase-separation of the material into a ferromagnetic metallic phase and a charge ordered antiferromagnetic insulating phase close to the magnetic transition temperature has been suggested as one of the mechanisms adding to the explanation of the CMR effect [10]. Neutron scattering experiments have shown the existence of magnetic clusters above T_C in $La_{1-x}Ca_xMnO_3$ [11, 12] and theoretical models using Monte Carlo simulations [13] have predicted the presence of phase-separation. In the phase-separation scheme, the CMR effect is

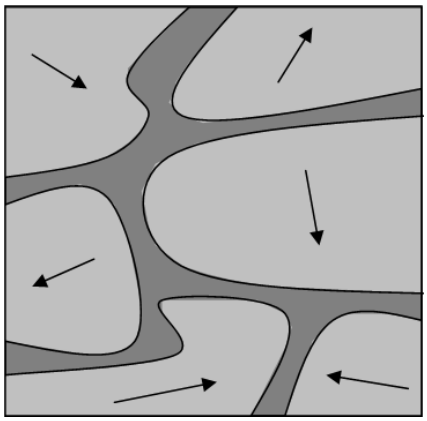

Figure 2.4: A representation of the phase-separated CMR state. The FM islands with randomly oriented magnetisation (light grey) are separated by walls of the competing insulating state (dark grey).

explained as follows: Close to T_C, the material consists of FM clusters with random orientation, separated by walls of the competing insulating state (figure 2.4). As a consequence of the double exchange mechanism, no hopping takes place between metallic clusters with different FM orientations and the material is in an insulating state. However, upon the application of an external magnetic field, the effective spin of the FM clusters will rotate and the insulating walls will melt, leading to a metallic state. The coexistence of clusters of different phases may result from the different hole densities of the competing states (the so-called "electronic phase-separation") [14, 15], or it may be disorder driven, with competing states of equal electron density leading to large coexisting clusters near a first-order phase transition [16]. While phase-separation seems to be a key factor in the explanation of the CMR effect, many questions, e.g. about the size and temperature evolution of the clusters, remain.

2.2 Charge order and phase-separation in $(Pr_{1-y}La_y)_{0.7}Ca_{0.3}MnO_3$

In manganites with a low tolerance factor, a charge or orbital ordered (CO/OO) state may be formed as the result of the deviation of the Mn−O−Mn bond angle from 180°. In a CO/OO state, the Mn^{3+}/Mn^{4+} ions and the 3d e_g orbitals form an ordered structure, and superexchange interactions may start to compete with the double exchange mechanism. The effect of the increased orthorhombic distortions of the crystal lattice are well visible in e.g. $Pr_{1-x}Ca_xMnO_3$, which shows a charge ordered insulating (COI) state below $220 - 240$ K for $x \geq 0.3$, and no ferromagnetic metallic (FMM) ground state at any x in zero field.

Upon substituting the Pr^{3+} ions in $Pr_{1-x}Ca_xMnO_3$ with larger La^{3+} ions, an electronically mixed state will form, consisting of clusters of charge ordered insulating and ferromagnetic metallic phases. Mixed compounds of $(Pr_{1-y}La_y)_{0.7}Ca_{0.3}MnO_3$ or compounds with a similar doping of $x \approx 0.3$ have been investigated as bulk ceramic phases [17, 18], single-crystals [19] and epitaxially grown films [20, 21, 22, 23, 24].

With increasing y, a transition from a largely CO insulating to a FM metallic state is observed, typically showing a kind of threshold behaviour where large changes in conductivity and magnetic transition temperature are observed near a specific composition (figure 2.5)) [17, 18, 25]. The coexistence of an antiferromagnetic CO and a FM phase has been detected and investigated by neutron scattering [26], electron diffraction in a transmission electron microscope [25, 27], magnetic force microscopy [23] and magneto-optical imaging [19]. The extension of the different phases in $(Pr_{1-y}La_y)_{0.7}Ca_{0.3}MnO_3$ may reach the micron range [19, 23, 25]. Electrical conduction proceeds via percolating conduction paths that can be visualised optically [28]. The metal-insulator transition, occurring during heating or cooling close to the magnetic transition temperature in the samples with a metallic ground state, has been proposed to be of a percolative nature [25, 29].

The coexistence of the charge ordered insulating and ferromagnetic metallic phases

in PLCMO or related Pr-manganites has been found to be sensitive to various external parameters such as electric and magnetic DC fields, light or x-rays [30], hydrostatic pressure [31] and epitaxial strain in thin films. The most well-known effect of an external parameter is the colossal magnetoresistance, a drop of the electrical resistance by several orders of magnitude under an applied magnetic field. But also an electric field or a current applied to insulating $(Pr_{1-y}La_y)_{0.7}Ca_{0.3}MnO_3$ or $Pr_{1-x}Ca_xMnO_3$ may induce a conducting state [19, 32], i.e. depending on the composition y, electrical conduction may be highly non-linear. Tokunaga *et al.* [19] magneto-optically observed fluctuations of the conduction path depending on the applied electric field, revealing the interaction of a spin-polarised current with the local magnetic state. The response of $Pr_{1-x}Ca_xMnO_3$ to hydrostatic pressure has been found to be rather complex, in the sense that the sign of the change in conductivity with pressure depends on the doping level [31]. Together, these observations lead to a complex phase diagram (figure 2.5).

Thin epitaxial films of phase-separated $(Pr_{1-y}La_y)_{1-x}Ca_xMnO_3$ in the doping range of $x = 0.3-0.375$ have been investigated by various groups [20, 21, 22, 23, 33]. Further work on e.g. $Pr_{1-x}(Ca,Sr)_xMnO_3$ films with $x = 0.3 - 0.4$ [32, 34] shows

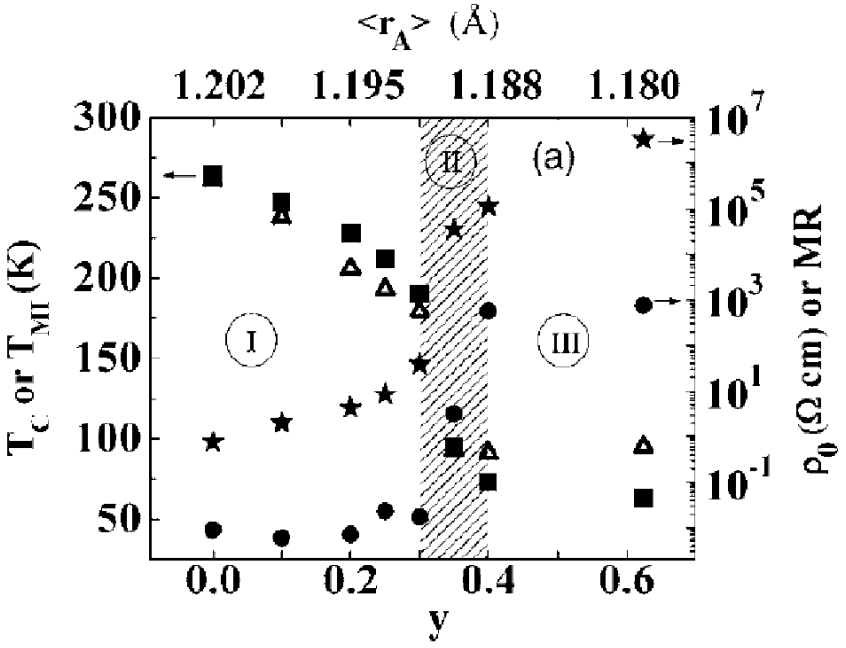

Figure 2.5: Phase diagram of bulk PLCMO from resistivity and magnetic susceptibility data. Shown are the metal-insulator transition temperature recorded during cooling ($T_{MI}^{cooling}$, squares), T_C (triangles), the resistivity (ρ_0, circles) and the magnetoresistance (MR, stars). The shaded area (II) denotes the threshold behaviour associated with the transition from a FMM (I) to a COI (III) ground state. Data reproduced from Masunaga *et al.* [17].

similar tendencies with respect to T_C and conduction behaviour in dependence on composition, since the ionic radius effect is utilised in a similar fashion. The behaviour of films that are thick enough for the finite size effect to be neglected, is subject to one crucial additional parameter: epitaxial strain in the film plane. It has been shown that the energy balance between the different phases can be controlled by choosing substrates with different lattice mismatch [20, 22, 35]. As a general tendency, tensile strain is found to stabilise a CO state in several reports [22, 35]. Keeping in mind the complex response of $Pr_{1-x}Ca_xMnO_3$ to hydrostatic pressure [31] however, there may be exceptions to this tendency.

2.3 The effect of strain on magnetisation

Epitaxial strain plays a key role in the properties of thin film manganites. One way to investigate the effect of strain is by growing films on various substrates with different lattice mismatch. The defect structures and oxygen content of the films, however, may vary depending on the substrate. The use of piezoelectric PMN-PT (001) $(PbMg_{1/3}Nb_{2/3}O_3)_{0.72}(PbTiO_3)_{0.28}$ as a substrate allows a biaxial compression of as-grown epitaxial films by as much as 0.2% [36, 37]. This reversible dynamic strain process gives a unique insight into the effect of strain on thin film manganites, eliminating undesired variations in microstructure which may occur when several substrates with different lattice mismatch are used. The reversible strain approach is especially useful for studies of transport properties such as the elastoresistance, since the comparison of samples on different substrates is unreliable due to different microstructures.

Specifically in the CMR manganites, the magnetic transition temperature has been found to be extremely sensitive to biaxial strain. A model by Millis *et al.* [38] describes the effect of biaxial strain ϵ_{xx} and ϵ_{yy} on the ordering temperature of the CMR manganites. In the model, T_C depends on two parameters: the bulk compression $\epsilon_B = 1/3(2\epsilon_{xx} + \epsilon_{zz})$ (assuming $\epsilon_{xx} = \epsilon_{yy}$), and the biaxial distortion $\epsilon^* = 1/2(\epsilon_{zz} - \epsilon_{xx})$, where $\epsilon_{xx} = (a_{xx} - a_{bulk})/a_{bulk}$ and $\epsilon_{zz} = (a_{zz} - a_{bulk})/a_{bulk}$ are the pseudocubic in-plane and out-of-plane strain. Within the model, the Curie temperature can be described as:

$$T_C(\epsilon_B, \epsilon^*) = T_C(0,0)(1 - \alpha\epsilon_B - \Delta(\epsilon^*)^2), \tag{2.2}$$

where $\alpha = (1/T_C)[(dT_C)/(d\epsilon_B)]$, $\Delta = (1/T_C)[(d^2T_C)/(d\epsilon^{*2})]$, and $\alpha, \Delta > 0$. $dT_C/d\epsilon^*$ is 0 in the cubic state. The parameter ϵ_B tends to increase the probability of the electron hopping, reducing the effect of the electron-lattice coupling. The biaxial distortion ϵ^*, will increase the Jahn-Teller splitting of the e_g electron levels and will cause a decrease in T_C. Millis *et al* predicted typical values for α and Δ in manganites to be around 6 and $1.4 \cdot 10^3$, respectively. In the case of $La_{0.7}Sr_{0.3}MnO_3$ films, considerable disagreement exists on the values of α and Δ [39, 40, 41]. However, all of the values were derived from data on samples with different thicknesses (i.e., different and often inhomogeneous strain conditions due to progressive strain

relaxation). A recent extensive study of $La_{0.7}Sr_{0.3}MnO_3$ thin films grown on eight different substrates revealed values of $T_C(0,0) = 345 \pm 9$ K, $\alpha = 1.55 \pm 0.01$, and $\Delta = 1460 \pm 30$ [42], in good agreement with the theoretical predictions.

2.4 Interface effects in [$La_{0.7}Sr_{0.3}MnO_3/SrTiO_3$] superlattices

Manganites have long been known for their colossal magnetoresistance effect and the large number of different ground states and phase transitions displayed in both bulk materials and thin films. Modern thin film deposition techniques, such as RHEED assisted pulsed laser deposition (see 3.1.2), have opened the door to another fascinating 'dimension': The precise tailoring of the crystal growth allows for the fabrication of atomically sharp interfaces between different materials. Well defined superlattice structures of different manganites can be grown, or the manganites can be combined with other perovskite type oxides in order to create material characteristics not found in bulk. Sometimes, unexpected features may arise, such as the conduction found at the interface between $LaAlO_3$ and $SrTiO_3$, two insulating materials with the perovskite structure [43].

Many studies have been focussed on $La_{0.7}Sr_{0.3}MnO_3$ (LSMO), which shows the highest Curie temperature among the manganites ($T_C \sim 370$ K). Thin films display different properties compared to bulk LSMO, and it is well known that substrate-induced lattice strain can cause structural modifications which strongly affect the magnetic properties. Besides a suppression of the ferromagnetic exchange mechanism and a reduction of the ferromagnetic transition temperature by tensile strain, it has been found that ultra-thin films of LSMO display a modified magnetic behaviour compared to thicker films. This finding led to the proposal of the existence of an interface layer which is insulating as well as magnetically disordered over the whole temperature range. As the origin of this so-called magnetically "dead" layer, a mixed phase state, with nanoscale electronically separated ferromagnetic metallic and charge/orbital ordered insulating clusters has been suggested [44, 45]. The electronic state of the interface layer is strongly strain dependent. The thickness of the interface layer varies too, depending on the lattice mismatch of the LSMO film with the substrate [46, 47, 48]. A recent study [49] of ultra thin films deposited on STO found that the LSMO layer stops being metallic below a critical thickness of ~ 32 Å. Below this critical thickness, T_C decreases rapidly and the spontaneous magnetisation plunges. These observations may be explained in the phase-separation scheme by the loss of a conducting percolation path for films thinner than ~ 32 Å. The measurements of the magnetisation show the behaviour of the isolated ferromagnetic metallic clusters.

Bibliography

[1] *Optical Conductivity of manganites: Crossover from Jahn-Teller Small Polaron to Coherent Transport in the Ferromagnetic State*, M. Quijada, J. Cerne, J.R. Simpson, H.D. Drew, K.H. Ahn, A.J. Millis, R. Shreekala, R. Ramesh, M. Rajeswari, T. Venkatesan, Phys. Rev B **58**, 16093-102 (1998)

[2] *Anomalous Variation of Optical Spectra with Spin Polarization in Double-Exchange Ferromagnet:* $La_{1-x}Sr_xMnO_3$, Y. Okimoto, T. Katsufuji, T. Ishikawa, A. Urushibara, T. Arima, and Y. Tokura, Phys. Rev. Lett. **75**, 109 (1995)

[3] *Considerations on Double Exchange*, P.W. Anderson, H. Hasegawa, Phys. Rev. **100**, 67 (1955)

[4] *Interaction between the d-Shells in the Transition Metals. II. Ferromagnetic Compounds of Manganese with Perovskite Structure*, C. Zener, Phys. Rev. **82**, 403 (1951)

[5] *Dynamic Jahn-Teller Effect and Colossal Magnetoresistance in* $La_{1-x}Sr_xMnO_3$, A.J. Millis, Boris I. Shraiman, R. Mueller, Phys. Rev. Lett. **77**, 175 (1996)

[6] *Cooperative Jahn-Teller effect and electron-phonon coupling in* $La_{1-x}A_xMnO_3$, A.J. Millis, Phys. Rev. B **53**, 8434 (1996)

[7] *Geochemische Verteilungsgesetze der Elemente VII, VIII*, V.M. Goldschmidt (1927-1928)

[8] *Ferromagnetic compounds of manganese with perovskite structure*, H.G. Jonker, J.H. van Santen, Physica **16**, 337 (1950)

[9] *Lattice Effects on the Magnetoresistance in Doped* $LaMnO_3$, H.Y. Hwang, S-W. Cheong, P.G. Radaelli, M. Marezio, B. Batlogg, Phys. Rev. Lett. **75**, 914 (1995)

[10] *X-Ray effects in charge-ordered manganites: a magnetic mechanism of persistent photoconductivity*, B. Keimer, D. Casa, V. Kiryukhin, O.A. Saleh, J.P. Hill, Y. Tomioka, Y. Tokura, Mater. Sci. Eng., B **63**, 30 (1999)

[11] *Evidence for magnetic polarons in the magnetoresistive perovskites*, J.M. De Teresa, M.R. Ibarra, P.A. Algarabel, C. Ritter, C. Marquina, J. Blasco, J. García, A. del Moral, Z. Arnold, Nature **386**, 256 (1997)

[12] *Liquidlike Spatial Distribution of Magnetic Droplets Revealed by Neutron Scattering in* $La_{1-x}Ca_xMnO_3$, M. Hennion, F. Moussa, G. Biotteau, J. Rodríguez-Carvajal, L. Pinsard, A. Revcolevschi, Phys. Rev. Lett. **81**, 1975 (1998)

[13] *Phase Separation Induced by Orbital Degrees of Freedom in Models for Manganites with Jahn-Teller Phonons*, S. Yunoki, A. Moreo, E. Dagotto, Phys. Rev. Lett. **81**, 5612 (1998)

[14] *Current ideas on the origin of stripes*, J. Zaanen. J. Phys. Chem. Solids **59**, 1769 (1998)

[15] *Stripe phases in high-temperature superconductors*, V.J. Emery, S.A. Kivelson, J.M. Tranquada, Proc. Natl. Acad. Sci. USA **96**, 8814 (1999)

[16] *Giant cluster coexistence in doped manganites and other compounds*, A. Moreo, M. Mayr, Ad. Feiguin, S. Yunoki, E. Dagotto, Phys. Rev. Lett. **84**, 5568 (2000)

[17] *Competition between coexisting phases in (La,Pr)*$CaMnO_3$ *manganites*, S.H. Masunaga, R.F. Jardim, J. Appl. Phys. **102**, 073903 (2007)

[18] *Comparative study of the magnetic phase diagrams of* $(La_{1-y}Pr_y)_{0.7}Ca_{0.3}MnO_3$ *with oxygen isotopes* ^{16}O *and* ^{18}O, A.M. Balagurov, V.Y. Pomjakushin, D.V. Sheptyakov, N.A. Babushkina, O.Y. Gorbenko, A.R. Kaul, Physica B (Amsterdam) **350**, 1 (2004)

[19] *Current oscillation and low-field colossal magnetoresistance effect in phase-separated manganites*, M. Tokunaga, H. Song, T. Tokunaga, T. Tamegai, Phys. Rev. Lett. **94**, 157203 (2004)

[20] *Substrate induced strain effects in epitaxial* $La_{0.67x}Pr_xCa_{0.33}MnO_3$ *thin films*, T. Wu, S.B. Ogale, A. Biswas, T. Poletto, R.L. Greene, T. Venkatesan, A.J. Millis, J. Appl. Phys. **93**, 5507 (2003)

[21] *Effect of strain and electric field on the electronic soft matter in manganite thin films*, T. Dhakal, J. Tosado, A. Biswas, Phys. Rev. B **75**, 092404 (2007)

[22] *Influence of different substrates on phase-separation in* $La_{1-x-y}Pr_yCa_xMnO_3$ *thin films*, D. Gillaspie, J.X. Ma, H.-Y. Zhai, T.Z. Ward, H.M. Christen, E.W. Plummer, J. Shen, J. Appl. Phys. **99**, 08S901 (2006)

[23] *Direct Observation of Percolation in a Manganite Thin Film*, L. Zhang, C. Israel, A. Biswas, R.L. Greene, A. de Lozanne, Science **298**, 805 (2008)

[24] *Colossal elastoresistance and strain-dependent magnetization of phase-separated* $(Pr_{1-y}La_y)_{0.7}Ca_{0.3}MnO_3$ *thin films*, M.C. Dekker, A.D. Rata, K. Boldyreva, S. Oswald, L. Schultz, K. Dörr, Phys. Rev. B **80**, 144402 (2009)

[25] *Percolative phase-separation underlies colossal magnetoresistance in mixed-valent manganites*, M. Uehara, S. Mori, C.H. Chen, S.-W. Cheong, Nature **10**, 87 (1998)

[26] *Signature of magnetic phase-separation in the ground state of* $Pr_{1-x}Ca_xMnO_3$, H. Sha, F. Ye, P. Dai, J.A. Fernandez-Baca, D. Mesa, J.W. Lynn, Y. Tomioka, Y. Tokura, J. Zhang, Phys. Rev. B **78**, 052410 (2008)

[27] *Experimental confirmation of Zener-polaron-type charge and orbital ordering in* $Pr_{1-x}Ca_xMnO_3$, L. Wu, R.F. Klie, Y. Zhu, Ch. Jooss, Phys. Rev. B **76**, 174210 (2007)

[28] *Visualization of the Local Insulator-Metal Transition in* $Pr_{0.7}Ca_{0.3}MnO_3$, M. Fiebig, K. Miyano, Y. Tomioka, Y. Tokura , Science **280**, 1925 (1998)

[29] *Colossal magnetoresistant materials: the key role of phase-separation*, E. Dagotto, T. Hotta, A. Moreo, Phys. Rep. **344**, 1-153 (2001)

[30] *An X-ray-induced insulator-metal transition in a magnetoresistive manganite*, V. Kiryukhin, D. Casa, J.P. Hill, B. Keimer, A. Vigliante, Y. Tomokia, Y. Tokura, Nature **386**, 813 (1997)

[31] *Pressure effects on charge, spin, and metal-insulator transitions in the narrow bandwidth manganite* $Pr_{1-x}Ca_xMnO_3$, C. Cui, T.A. Tyson, Phys. Rev. B **70**, 094409 (2004)

[32] *Electric- and magnetic-field-driven nonlinear charge transport and magnetic ordering in epitaxial films of* $Pr_{0.7}Ca_{0.3-x}Sr_xMnO_3$, R.C. Budhani, N.K. Panday, P. Padhan, S. Srivastava, R.P.S. Lobo, Phys. Rev. B **65**, 014429 (2001)

[33] *Comparative study of magnetic and electric field induced insulator-metal-transitions in* $Pr_{1-x}Ca_xMnO_3$ *films*, W. Westhäuser, S. Schramm, J. Hoffmann, C. Jooss, Eur. Phys. J. B **53**, 323 (2006)

[34] *Persistent and Reversible All-Optical Phase Control in a Manganite Thin Film*, N. Takubo, Y. Ogimoto, M. Nakamura, H. Tamaru, M. Izumi, K. Miyano, Phys. Rev. Lett. **95**, 017404 (2005)

[35] *High magnetic field transport measurements of charge-ordered* $Pr_{0.5}Ca_{0.5}MnO_3$ *strained thin films*, W. Prellier, E.R. Buzin, Ch. Simon, B. Mercey, M. Hervieu, S. de Brion, G. Chouteau, Phys. Rev. B **66**, 024432 (2002)

[36] *Voltage-controlled epitaxial strain in $La_{0.7}Sr_{0.3}MnO_3/Pb(Mg_{1/3}Nb_{2/3})O_3$-$PbTiO_3$(001) films*, C. Thiele, K. Dörr, S. Fähler, L. Schultz, D. C. Meyer, A.A. Levin, P. Paufler, Appl. Phys. Lett. **87**, 262502 (2005)

[37] *Reversible uniform strain in epitaxial oxide films*, M.D. Biegalski, K. Dörr, D.-H. Kim, H.M. Christen, unpublished

[38] *Quantifying strain dependence in "colossal" magnetoresistance manganites*, A.J. Millis, T. Darling, A. Migliori, J. Appl. Phys. **83**, 1588 (1998)

[39] *Strain-dependent magnetic phase diagram of epitaxial $La_{0.67}Sr_{0.33}MnO_3$ thin films*, F. Tsui, M.C. Smoak, T.K. Nath, C.B. Eom, Appl. Phys. Lett. **76**, 2421 (2000)

[40] *Strain-induced magnetic anisotropy in epitaxial manganite films*, L. Ranno, A. Llobet, R. Tiron, E. Favre-Nicolin, Appl. Surf. Sci. **188**, 170 (2002)

[41] *Suppression of the metal-insulator transition temperature in thin $La_{0.7}Sr_{0.3}MnO_3$ films*, M. Angeloni, G. Balestrino, N. G. Boggio, P. G. Medaglia, P. Orgiani, A. Tebano, J. Appl. Phys. **96**, 6387 (2004)

[42] *Effect of biaxial strain on the electrical and magnetic properties of (001) $La_{0.7}Sr_{0.3}MnO_3$ thin films*, C. Adamo, X. Ke, H.Q. Wang, H.L. Xin, T. Heeg, M.E. Hawley, W. Zander, J. Schubert, P. Schiffer, D.A. Muller, L. Maritato, D.G. Schlom, Appl. Phys. Lett. **5**, 112504 (2009)

[43] *A high-mobility electron gas at the $LaAlO_3/SrTiO_3$ heterointerface,* A. Ohtomo, H.Y. Hwang, Nature (London) **427**, 423 (2004)

[44] *Electronic phase-separation in manganite-insulator interfaces*, L. Brey, Phys. Rev. B **75**, 104423 (2007)

[45] *Charge trapping in optimally doped epitaxial manganite thin films*, M. Bibes, S. Valencia, L. Balcells, B. Martínez, J. Fontcuberta, M. Wojcik, S. Nadolski, E. Jedryka, Phys. Rev. B **66**, 134416 (2002)

[46] *Thickness-dependent magnetotransport in ultrathin manganite films*, J.Z. Sun, D.W. Abraham, R.A. Rao, C.B. Eom, Appl. Phys. Lett. **74**, 3017 (1999)

[47] *Suppression of the metal-insulator transition temperature in thin $La_{0.7}Sr_{0.3}MnO_3$ films*, M. Angeloni, G. Balestrino, N.G. Boggio, P.G. Medaglia, P. Orgiani, A. Tebano, J. Appl. Phys. **96**, 6387 (2004)

[48] *Magnetic and electric "dead" layers in $La_{0.7}Sr_{0.3}MnO_3$ thin films*, R.P. Borges, W. Guichard, J.G. Lunney, J.M.D. Coey, F. Ott, J. Appl. Phys. **89**, 3868 (2001)

[49] *Critical thickness and orbital ordering in ultrathin $La_{0.7}Sr_{0.3}MnO_3$ films*, M. Huijben, L.W. Martin, Y.-H. Chu, M.B. Holcomb, P. Yu, G. Rijnders, D.H.A. Blank, R. Ramesh, Phys. Rev. B **78**, 094413 (2008)

Chapter 3

Thin film preparation

3.1 Pulsed laser deposition

All films described in this work have been deposited by pulsed laser deposition (PLD). PLD is a conceptually and experimentally simple tool for the fabrication of thin films and multilayers. Its advantages for the growth of chemically complex oxides include stoichiometric transfer, reactive deposition and the possibility to grow artificially layered structures. In situ monitoring techniques, such as reflection high energy electron diffraction (RHEED), provide information about the surface morphology and the growth rate during film growth.

3.1.1 Basic principles of PLD

In PLD, a high energy laser is used to ablate material from a target. The ablated material is then transferred stoichiometrically onto a substrate. In the process of laser ablation, the photons hitting the target are first converted into electronic excitations, then into thermal, chemical and mechanical energy [1, 2], resulting in the rapid removal of material from the surface of the target. When the photons hit the target, they are absorbed in a shallow layer near the surface, which results in a dense layer of vapour in front of the target. The penetration depth of the photons depends on the laser wavelength, and should not be too high in order to avoid subsurface boiling, which will result in the formation of particulates. For relatively long pulse durations, such as the tens of nanoseconds typical for excimer lasers (KrF 248 nm, pulse duration typically 20-50 ns), a strong interaction between the forming plasma plume and the incident beam results in further heating and partial ionisation of the vapour. The resulting high pressure will expand the plasma from the target surface in the direction of the substrate. The kinetic energy of the ablated particles will vary depending on the background pressure and the species (ions, electrons and neutral atoms travel at different velocities). If a background gas, such as argon or oxygen, is used, the ablated particles interact with the gas before hitting the substrate. Assuming that most species in the plasma plume should be fully thermalised at the time they reach the substrate (i.e. having equal forward and lateral velocities), a simple model predicts that the optimal growth rate of oxides should be close to 1 Å per

pulse [3]. For the precise formation of superlattices and particulate-free perovskites, however, much lower deposition rates are required [4]. Once the ablated particles have reached the substrate surface, surface diffusion and the absortion/desorption probabilities of the adatoms can be controlled by the substrate temperature.

One of the great advantages of PLD is the stoichiometric transfer of target material onto the substrate. However, not all elements are incorporated into the growing film at the same rate and the more volatile elements may re-evaporate from the substrate surface. When growing oxide materials, an additional source of oxygen is needed for proper control of the oxygen content.

Since each laser pulse results in the deposition of far less than a monolayer of material on the substrate, PLD can be utilised to form alloys by the sequential ablation of material from multiple targets. A multi-target carousel can be used for this purpose, simply by exchanging the target before a full monolayer of material has formed. Heterostructures or superlattices are formed using a conceptually similar approach, except that at least one complete layer is deposited before switching to the next material. In order to grow a true superlattice, however, the roughness of each interface must be significantly smaller than the thickness of the layers.

The simplest approach to multilayer fabrication is to calibrate the growth rates for each material (in terms of the amount of material deposited per laser pulse) and then grow the superlattice by counting laser pulses. Alternatively, RHEED can be used to track the number of deposited layers in real time.

3.1.2 Reflection high energy electron diffraction

In order to precisely tailor film properties such as surface roughness, interface properties and phase stability, a good understanding of the basic processes and mechanisms of the growth of complex oxides is of principal importance. The growth of thin films from atoms deposited from the gas phase is intrinsically a non-equilibrium phenomenon governed by a competition between kinetics and thermodynamics. The most important kinetic mechanisms of film growth include nucleation, adatom diffusion, and the attachment and detachment of adatoms to terraces and islands. Reflection high energy electron diffraction (RHEED) provides information about the periodic arrangement of the atoms and the evolution of the growth front during thin film deposition. *In-situ* analysis of the structural properties helps to control the surface morphology and the crystal structure of the film during growth.

For RHEED, the information comes from a diffraction pattern formed by monoenergetic electrons scattering off the crystal surface. The wavelength λ of the electrons can be estimated by the de Broglie relation as:

$$\lambda = \frac{h}{p} = \sqrt{\frac{h^2}{2mE}}, \tag{3.1}$$

where h is the Planck constant and p the momentum, or

$$\lambda \text{ (in Å)} = \sqrt{\frac{150}{E \text{ (in eV)}}}, \tag{3.2}$$

where λ is the wavelength of the electrons in Å and E is the energy in eV. At the energies used in RHEED ($10 - 50$ keV), this corresponds to an electron wavelength between 0.05 and 0.1 Å. At a grazing incidence angle of $\theta_i = 0.1 - 5°$, the electrons interact with the topmost atomic layers ($1 - 2$ nm) only, making RHEED a surface sensitive technique. The diffraction pattern of the scattered electrons contains information on the crystal structure and morphology of the film surface.

In order for the electrons to form a constructive interference pattern, energy and momentum conservation give the requirements:

$$|\mathbf{k}_f| = |\mathbf{k}_i| \tag{3.3}$$

and

$$\mathbf{k}_f - \mathbf{k}_i = \mathbf{G}, \tag{3.4}$$

where $\mathbf{k}_i$ and $\mathbf{k}_f$ are the incident and the final electron wave vectors respectively, and $\mathbf{G}$ is a vector of the reciprocal lattice. Equation 3.3 requires that the locus of all final wave vectors is a sphere, the so-called Ewald sphere, while the conservation of momentum in a crystal demands that the $\mathbf{k}$-vectors differ by a reciprocal lattice vector $\mathbf{G}$ (equation 3.4). The intersection of the Ewald sphere with the reciprocal lattice points determines which diffraction conditions are allowed. In RHEED, because the incoming electrons interact with the topmost atomic layers only, the reciprocal lattice consists of a family of parallel rods, resulting in diffraction spots lying on concentric circles, the so-called Laue circles.

In addition to the diffraction pattern formed by the elastically scattered electrons, one can also discern features of inelastically scattered electrons, the so-called Kikuchi lines. Many inelastically scattered electrons, however, cannot be distinguished from the elastic ones, and contribute significantly to the total detected intensity.

Another reason RHEED is popular in combination with pulsed laser deposition is the observation of intensity oscillations of the specular beam during deposition [6]. Intuitively, the intensity oscillations can be understood by considering a layer-by-layer growth front. Material deposited on an initially flat surface leads to roughening and a decrease in the intensity. When more material is deposited to complete the forming crystal layer, surface smoothing leads to an increase in intensity. Accordingly, RHEED can be used as a thickness monitor, since the oscillation period of the intensity corresponds to the deposition of a single crystal layer.

3.2 PLD chamber setup

The films investigated in this work have been grown in two different PLD chambers. In one chamber, $(Pr,La)_{0.7}Ca_{0.3}MnO_3$ alloys with various Pr/La ratios have been

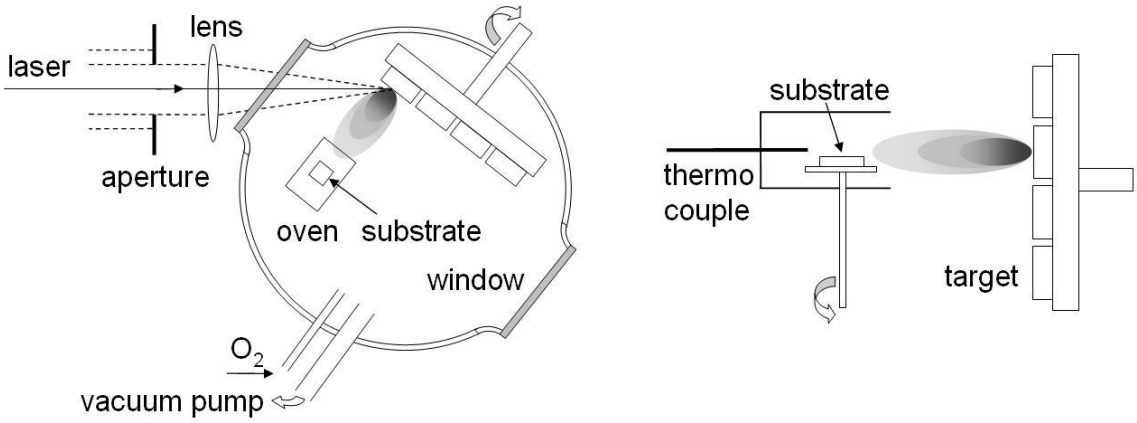

Figure 3.1: Schematic of the PLD setup of chamber 1 and a side view showing off-axis deposition.

grown by sequential ablation from a $La_{0.7}Ca_{0.3}MnO_3$ and a $Pr_{0.7}Ca_{0.3}MnO_3$ target. In the same chamber, [$La_{0.7}Sr_{0.3}MnO_3$ / $SrTiO_3$] superlattices have been deposited on $SrTiO_3$ and piezoelectric PMN-PT substrates. A second chamber, equipped with a RHEED facility, has been used for the more precisely controlled growth of [$La_{0.7}Sr_{0.3}MnO_3$ / $SrTiO_3$] superlattices on $SrTiO_3$.

All films were deposited using a KrF excimer laser (Lambda Physik LPX305i, $\lambda = 248$ nm), with a pulse duration τ of $20 - 50$ ns and a maximum pulse frequency f of 50 Hz. Before entering the chamber, the laser light is lead through an aperture to select the homogeneous part of the gaussian light profile only. The aperture is then projected onto the target by a focussing lens, which can be used to adjust the energy density on the target. Both chambers contain a target carousel, on which up to 6 targets can be mounted.

In chamber 1, films were grown in the so-called off-axis geometry [5] (figure 3.1), where the substrate is tilted under an angle of 90 degrees to the target surface. The advantage of off-axis deposition is that only fully thermalised particles are deposited on the substrate surface, avoiding larger agglomerates detrimental to the formation of a single-crystalline film. In order to assure an even distribution of incoming particles on the substrate surface, the substrate holder is rotated during deposition. The substrate is heated in a cylindrical oven, which reaches temperatures up to 820° C. A rotary pump is used to create a base pressure of $p_B = 10^{-3}$ mbar, while the films are grown in an oxygen background pressure of $p_{O_2} = 1.5 - 4.5 \cdot 10^{-1}$ mbar. The laser energy lies between 450 and 525 mJ, with a pulse frequency of 2-3 Hz, resulting in a growth rate of $0.1 - 0.2$ Å per pulse. The exact deposition conditions for the different materials are summarised in table 3.1.

In chamber 2, [$La_{0.7}Sr_{0.3}MnO_3$ / $SrTiO_3$] superlattices have been grown in standard on-axis geometry, using *in-situ* RHEED analysis of the crystal surfaces. The $SrTiO_3$ substrates were glued onto the heater element with silver paste. The vacuum chamber was then pumped to a base pressure of $10^{-5} - 10^{-6}$ mbar by a turbo

pump. The films were grown in an oxygen background pressure of 0.3 mbar, with a pulse frequency of 3 Hz and a laser energy density of 1.25 J/cm^2. The growth rate was approximately 0.05 Å per pulse. The surface morphology of the growing films was checked by a high pressure RHEED system (see e.g. [7] for details), placed perpendicular to the target-substrate axis. After exiting the filament, the electrons were accelerated with energies between 25 and 30 keV, resulting in an electron beam of several 100 μm diameter [8]. After refraction, the electrons were caught on a fluorescent phosphor screen, and the diffraction pattern was recorded by a CCD camera connected to a computer. The RHEED patterns have been recorded and analysed with K-Space Associates acquisition software (KSA400, v.4.79).

Chamber 1				
Film	Substrate	T (°)	p_{O_2} (mbar)	f (Hz)
PLCMO	STO	725	$3.0 \cdot 10^{-1}$	2
PLCMO	PMN-PT	725	$3.0 \cdot 10^{-1}$	2
LSMO/STO	STO	700	$4.5 \cdot 10^{-1}$	3
LSMO/STO	PMN-PT	700	$4.5 \cdot 10^{-1}$	3
Chamber 2				
Film	Substrate	T (°)	p_{O_2} (mbar)	f (Hz)
LSMO/STO	STO	650	$3.0 \cdot 10^{-1}$	3

Table 3.1: Deposition conditions of the various samples in the off-axis chamber (1) and the RHEED chamber (2). T denotes the growth temperature, p_{O_2} the oxygen background pressure and f the pulse frequency of the laser.

Bibliography

[1] *Laser-induced phase explosion: new physical problems when a condensed phase approaches the thermodynamic critical*, A. Miotello, R. Kelly, Appl. Phys. A **69**, S67 (1999)

[2] *Pulsed Laser Deposition of Thin Films*, R. Kelly, A. Miotelly, ed D.H. Chrisey, G.K. Hubler, New York: Wiley (1994)

[3] *Pulsed laser deposition of oxides: Why the optimum rate is about 1 Å per pulse*, M. Strikovski, J.H. Miller Jr., Appl. Phys. Lett. **73** (12), 1733 (1998)

[4] *Strong polarization enhancement in asymmetric three-component ferroelectric superlattices*, H.N. Lee, H.M. Christen, M.F. Chisholm, C.M. Rouleau, D.H. Lowndes, Nature **433**, 395 (2005)

[5] *Off-axis laser deposition of* $YBa_2Cu_3O_{7-\delta}$ *thin films*, B. Holzapfel, B. Roas, L. Schultz, P. Bauer, G. Saemann-Ischenko, Appl. Phys. Lett. **61**, 3178 (1992)

[6] *Dynamics of film growth of GaAs by MBE from Rheed observations*, J.H. Neave, B.A. Joyce, P.J. Dobson, N. Norton, Appl. Phys. A **31**, 1 (1983)

[7] *Artificially layered oxides by pulsed laser deposition*, G. Koster, PhD thesis, Printpartners Ipskamp, Enschede (1999)

[8] *Intrinsic giant magnetoresistance of mixed valence La-A-Mn oxide (A=Ca,Sr,Ba)*, R. von Helmolt, J. Wecker, K. Samwer, L. Haupt, K. Bärner, J. Appl. Phys. **76**, 6925 (1994)

Chapter 4

Characterisation

This chapter describes the methods used to characterise the various films. In particular, the analysis of the crystal structure by x-ray diffraction and of the film growth by reflection high energy electron diffraction are described, as well as the use of piezoelectric substrates to reversibly strain and relax the films.

4.1 Crystal structure, interface sharpness and thickness

4.1.1 Characterisation by x-ray diffraction

When electromagnetic radiation falls on periodic structures with geometrical variations on the length scale of the radiation, diffraction effects are observed. The interatomic distances in molecules and crystals amount to $0.15 - 0.4$ nm, which correspond to the wavelength of x-rays having photon energies between 3 and 8 keV. At the relevant energy range, three different types of interaction are possible between x-rays and matter. The first two, photoionisation and Compton scattering, are inelastic scattering processes, where energy and momentum transfer from the incoming radiation to the exited electron may or may not release the electrons from their bound atomic states. Thirdly, x-rays may be scattered elastically by the electrons in a process called Thompson scattering, where the electron oscillates like a Hertz dipole at the frequency of the incoming beam and becomes a source of dipole radiation. It is the Thompson component in the scattering of x-rays that is made use of in the structural investigations by x-ray diffraction.

The x-ray measurements have been performed in a Siemens D5000 diffractometer using Co Kα radiation with a wavelength of $\lambda = 1.79$ Å ($\theta - 2\theta$ scans) and a Philips X'pert four circle diffractometer with Cu Kα radiation, $\lambda = 1.54$ Å (XRR and RSM).

XRD X-ray diffraction (XRD) $\theta - 2\theta$ scans in Bragg-Brentano geometry have been systematically employed to determine the crystallinity and out of plane lattice parameters of the films. From the $\theta - 2\theta$ diffraction pattern, the c lattice parameter of the film can be calculated:

$$n\lambda = 2d_{hkl}\sin(\theta) \tag{4.1}$$

where n is any integer, λ the wavelength, $d_{hkl} = c/\sqrt{h^2+k^2+l^2}$, c the lattice parameter and hkl the Miller indices.

For the [LSMO/STO] superlattices, the $\theta - 2\theta$ reflection pattern shows additional peaks, which can be thought of as a constructive interference of the thickness fringes from successive bi-layers of the superlattice structure. From the distance of these satellite peaks, the period of the superlattice Λ can be calculated:

$$\Lambda = \frac{(L_i - L_j)\lambda}{2(\sin(\theta_i) - \sin(\theta_j))}, \tag{4.2}$$

where L_i and L_j are two diffraction orders and θ_i and θ_j the angles at which these orders appear.

XRR For x-ray reflectivity (XRR) measurements, the diffractometer is used in the $\theta - 2\theta$ configuration, but with much smaller θ angles, typically between 0 and 5 degrees. Below a critical angle θ_c total reflection of the x-ray beam occurs. For $\theta > \theta_c$, intensity oscillations, called Kiessig oscillations or Kiessig fringes, can be seen. Maxima in the intensity are observed whenever the phase difference between the reflected and the refracted beam is a multiple of the wavelength λ. From the distance between adjacent Kiessig fringes $2\theta_{m+1}$ and $2\theta_m$ sufficiently above θ_c, the thickness t of the sample can be calculated via:

$$t \approx \frac{2\theta_{m+1} - 2\theta_m}{\lambda}. \tag{4.3}$$

Due to the roughness of the surface and the interfaces, thickness values of films above 100 nm are difficult to measure using Cu Kα radiation.

In XRR measurements of a superlattice system, the incident beam intensity is reduced by the reflection at the interfaces and the absorption in individual layers. The calculation of the reflected beam intensity was first described by Parratt in 1954 [1]. The position of the large interference maxima in the reflectivity curve caused by the superlattice peaks is described by:

$$\theta_m^2 = \langle\theta_c\rangle^2 + (\frac{\lambda}{2\Lambda})^2 m^2, \tag{4.4}$$

where $\langle\theta_c\rangle$ is the average critical angle of the total superlattice.

Between the interference maxima, small Kiessig fringes can be seen, scaling with the total thickness $N\Lambda$ of the superlattice. Ideally, there are $N-2$ fringes between two adjacent superlattice peaks. The thickness values for the individual layers A and B and the interface roughness σ_{AB} and σ_{BA} can be determined by fitting the reflected beam intensity, using a matrix technique approach as described by Gibaud and Hazra [2].

RSM Four-circle diffractometers give a high enough resolution to resolve closely adjacent features in reciprocal space. This makes it possible to characterise films by

reciprocal space mapping where, instead of running a line scan along Q_z, as is the case for a $\theta - 2\theta$ scan, the scattering intensity distribution of a reciprocal area Q_x, Q_z can be obtained by joining together successive one-dimensional scans in Q space. These can be either various rocking curve scans with increasing scattering angle 2θ or successive radial scans. RSM has the advantage that lattice misfits and the degree of relaxation can be obtained independent of the scanning ratio between ω and 2θ and the miscut of the diffracting plane with respect to the surface. The difference in the a and c lattice parameters between the film and the substrate appears as a peak separation between the reciprocal lattice points of the layer and the substrate along the Q_z and Q_x axis, respectively. From the lattice mismatch δ between the film and the substrate as found by RSM, the a and c lattice parameters of the film can be calculated via:

$$\delta_a = \frac{a_f - a_S}{a_S} \text{ and } \delta_c = \frac{c_f - a_S}{a_S}, \tag{4.5}$$

where a_f and c_f are the in-plane and out-of-plane lattice parameters of the film and a_S is the pseudo-cubic bulk lattice parameter of the substrate.

The degree of relaxation R of the film may be expressed in terms of the measured in-plane lattice parameter:

$$R = \frac{a_f - a_S}{a_B - a_S}, \tag{4.6}$$

where a_B is the pseudo-cubic bulk lattice parameter of the film. $R = 0$ if $\delta_a = 0$ and the film is fully strained on the substrate. If $R = 1$, $a_f = a_B$ and the film is fully relaxed.

4.1.2 *In-situ* characterisation by RHEED

Reflection high energy electron diffraction (RHEED) is a method to get structural information during film growth. Using a setup like the one described in section 3.2, the lattice parameters d_x (parallel to incident beam) and d_y (perpendicular to incident beam) of the growing film can be determined from the angles θ_i and θ_f of the incoming and scattered beam with respect to the surface via:

$$n/d_x = 1/\lambda(\cos(\theta_f) - \cos(\theta_i)) \tag{4.7}$$

and

$$n/d_y = 1/\lambda(\cos(\theta_f)\sin(\phi_f)), \tag{4.8}$$

where n is the order of the reflection and ϕ_f is the azimuth of the scattered beam. Assuming that the angles are small enough, they can be determined directly from the relative on-screen distances divided by the sample-to-screen distance.

The RHEED pattern recorded during the deposition contains information on the structure of the growing film. Crystal defects, for example, such as the occurrence of more than one crystallographic domain, may change the position of the RHEED spots. Furthermore, a broadening of the spots or the appearance of streaks during

the growth is a qualitative measure of an increasing film roughness: a rough surface, for instance one consisting of randomly distributed terraces and steps, has broader lattice rods. The intersections of the broadened rods with the Ewald sphere appear in the RHEED image as streaks. Penetration of the electron beam through 3D islands results in transmission spots: the reciprocal lattice rods are replaced by the bulk reciprocal lattice, and the streaks are replaced by spots.

4.1.3 Surface morphology

To characterise the surface morphology of the films, an atomic force microscope (AFM, Digital Instruments Nanoscope III) was used in tapping mode. An AFM consists of a silicon or silicon nitride cantilever with a sharp tip, with a radius of curvature in the order of nanometres, at the end. In tapping mode, the cantilever is driven to oscillate near its resonance frequency (amplitude typically 100 to 200 nm) and brought close to the sample surface. Forces acting on the tip (e.g. Van der Waals force, dipole-dipole interaction, etc.) change the resonance frequency of the cantilever, causing the amplitude of the oscillation to decrease. The tip is then scanned over the sample surface while its height is adjusted to maintain a set cantilever oscillation amplitude. The resulting map of the scanned area represents the topology of the sample.

As a measure of the surface roughness of the films, the root mean square roughness σ has been calculated from the measured height $z(x, y)$ via:

$$\sigma = \sqrt{\frac{\sum_{n=1}^{N}(z_n - \overline{z})^2}{N-1}} \text{ with the average height } \overline{z} = \frac{\sum_{n=1}^{N} z_n}{N}, \tag{4.9}$$

for N data points with height z_n.

4.1.4 Thickness

The thickness of the PLCMO films grown on STO has been determined using a DekTak profilometer to measure the step height after etching away a small strip of film along the substrate edge. A solution of 1 vol.-% H_2SO_4 and 30 vol.-% H_2O_2 was used to selectively etch the manganite films, while leaving the STO substrate intact. The thickness of the PLCMO films grown on PMN-PT is assumed to be comparable to the thickness of the films on STO grown under the same conditions and with the same number of laser pules.

The total thickness of the [LSMO/STO] superlattices was calculated from the superlattice period Λ determined from $\theta-2\theta$ x-ray reflection measurements in Bragg-Brentano geometry (see 4.1.1).

4.1.5 Stoichiometry

Compositions of the PLCMO films on PMN-PT have been analysed by x-ray photoelectron spectroscopy (XPS) measurements (system PHI 5600 CI, Physical Electronics) for 6 different Pr concentrations. XPS spectra are obtained by irradiating a material with a focussed x-ray beam while measuring the kinetic energy and the number of electrons that escape from the top layer ($1-10$ nm) of the material. The binding energy of the emitted electrons E_b can be calculated via:

$$E_b = E_p - (E_k + \phi), \tag{4.10}$$

where E_p is the energy of the photons being used, E_k is the kinetic energy of the measured electrons and ϕ is the work function of the spectrometer.

Since every element produces a characteristic set of XPS peaks at characteristic binding energy values, the number of detected electrons is directly proportional to the number of atoms of that element within the area irradiated. To measure the composition throughout the films, a thin layer of material is sputtered away, after which the measurement is repeated until the substrate is reached.

The XPS measurements were carried out using non-monochromatic Kg-Kα x-ray radiation and 3.5 keV Ar^+ ions (2 mm $\times$ 2 mm scan size) for sputtering depth profiling. Atomic concentrations were calculated from the peak intensities using single element sensitivity factors.

4.2 Reversible substrate strain

To carry out strain-dependent measurements on the films grown on piezoelectric PMN-PT (001) $(PbMg_{1/3}Nb_{2/3}O_3)_{0.72}(PbTiO_3)_{0.28}$ substrates, a voltage $V \leq 300$ V was applied along the substrate normal between the film on top and a NiCr/Au electrode on the bottom (001) face of the PMN-PT, producing an electric field of $E \leq 10$ kV cm^{-1} in the 0.3 mm thick substrate. The resulting current is lower than 10^{-7} A after the crystal has been poled. The huge resistivity of the substrate ($> 10^{10}$ Ωcm) guarantees proper functioning of the manganite film as an upper electrode within the measurable range of film resistances. The electric field in the film resulting from the substrate voltage can be estimated as E times the ratio of the resistivities of the film and the substrate. For the measured range of film resistivities, this ratio is below 10^{-8}. The PMN-PT substrate shrinks approximately linearly with increasing E in both in-plane directions [3]. The maximum field of 10 kV cm^{-1} leads to an 0.11 % compression of the in-plane lattice parameter between 300 K and 90 K [3, 4]. The strain response of the PMN-PT substrate at temperatures below 90 K is taken to be equivalent to the 90 K response, due to lack of exact strain data at low temperatures. Since some strain reduction may occur towards low temperatures, the effect of the reversible substrate strain on the physical properties of the films may be systematically underestimated.

4.3 Physical properties

4.3.1 Magnetisation

The magnetisation M of the PLCMO films and the [LSMO/STO] superlattices has been determined using a superconducting quantum interference device (SQUID, Quantum Design, 5T). SQUIDs are based on the DC Josephson effect and have two Josephson junctions in parallel in a superconducting loop. When a small amount of external flux is applied to the superconducting loop, screening currents generate a magnetic field to cancel the applied external flux. The current in both branches of the loop flows in opposite directions and has a value of $I = I_{input} + I_S/2$ and $I = I_{input} - I_S/2$. If the current in either of the branches exceeds the critical current for the Josephson junction, the superconducting ring becomes resistive and a voltage appears across the junction. If the external flux is increased further to exceed $\Phi_0/2$, the screening current will start to flow in the opposite direction, in order to increase the flux quantum to an integral number. The screening current will change direction every time the flux increases by $\Phi_0/2$, and so the critical current oscillates as a function of applied flux. If the input current is higher than the critical current, the SQUID is operated in resistive mode and the voltage is a function of the applied magnetic field with a period equal to Φ_0. The change in flux $\Delta\Phi$ can be estimated from:

$$\Delta\Phi = (R/L)/\Delta V, \tag{4.11}$$

where R is a shunt resistance connected across the junction to eliminate a hysteresis of the current-voltage characteristics of the SQUID, L the self inductance of the superconducting ring, and ΔV the measured change in voltage.

The magnetisation M has been measured in dependence on temperature, magnetic field and reversible substrate strain. The Curie temperature has been estimated by extrapolating the linear part of the square of the magnetisation curve $M^2(T)$ to $M = 0$.

Strain dependent measurements have been conducted using a sample holder with additional voltage contacts at the sample position. The wires connected to the contacts have been lead through the holder past the sample, to a point below the measuring area of the SQUID, to avoid the influence of any current ($I_{piezo} < 5\mu$A) close to the sample during the measurements. The magnetisation of the NiCr/Au electrode of the PMN-PT can be neglected compared to the signal from the manganite films.

4.3.2 Resistance

Transport measurements of the PLCMO samples in dependence on temperature, magnetic field and reversible substrate strain have been carried out in four-probe geometry in both a cryostat equipped with a superconducting magnet and a cryogen-free refrigerator cryostat. A sufficiently low measuring current of I $\leq$ 10 μA was chosen so that the films showed Ohmic behaviour and no field- or current- induced

conductivity variations. Measurements have been done in a temperature range from 10 K to 300 K in magnetic fields up to 7 T.

Bibliography

[1] *Surface Studies of Solids by Total Reflection of X-Rays*, L.G. Parratt, Phys. Rev. **95**, 359 (1954)

[2] *X-ray reflectivity and diffuse scattering*, A. Gibaud, S. Hazra, Curr. Sci. **78**, 1467 (2000)

[3] *Influence of strain on the magnetization and magnetoelectric effect in* $La_{0.7}A_{0.3}MnO_3$ */ PMN-PT(001) (A=Sr,Ca)*, C. Thiele, K. Dörr, O. Bilani, J. Rödel, L. Schultz, Phys. Rev. B **75**, 054408 (2007)

[4] *Reversible uniform strain in epitaxial oxide films*, M.D. Biegalski, K. Dörr, D.-H. Kim, H.M. Christen, unpublished

Chapter 5

Phase-separated $(Pr,La)_{0.7}Ca_{0.3}MnO_3$ thin films

$(Pr_{1-y}La_y)_{0.7}Ca_{0.3}MnO_3$ (PLCMO) is an electronically phase-separated material consisting of clusters of a ferromagnetic (FM) metallic and a charge ordered (CO) insulating phase. The volume fractions of the different phases, and thus the physical properties of the material, are very sensitive to structural changes. The material's parent compounds, $Pr_{0.7}Ca_{0.3}MnO_3$ (PCMO) and $La_{0.7}Ca_{0.3}MnO_3$ (LCMO), have a charge ordered insulating and a ferromagnetic metallic ground state respectively. In this work, the composition y has been scanned to find the metal-insulator phase boundary for thin films of PLCMO grown on STO and PMN-PT substrates. Using the piezo-electric PMN-PT substrates, the effect of strain on the magnetisation and the electrical resistance, i.e. the so-called elastoresistance, of the PLCMO has been measured for films with different volume fractions of the FM metallic and the CO insulating phases.

5.1 Growth

Using the PLD setup described in section 3.2, $(Pr_{1-y}La_y)_{0.7}Ca_{0.3}MnO_3$ films of various Pr/La ratios have been deposited on STO and PMN-PT substrates by alternate ablation from stoichiometric targets of $Pr_{0.7}Ca_{0.3}MnO_3$ (PCMO) and $La_{0.7}Ca_{0.3}MnO_3$ (LCMO). All films have a thickness of 100 nm and were deposited under an oxygen pressure of $p = 0.3$ mbar, at a substrate temperature of $T = 725°C$ and with a pulse frequency of $f = 2$ Hz. To deposit one unit cell layer of film, 30 pulses were required. To grow a film with a La content y, $30y$ pulses of LCMO and $30(1-y)$ pulses of PCMO were cyclically ablated until the desired thickness was reached. Films have been grown with La concentrations of $y = 0, 0.2, 0.5, 0.55 - 0.65$ in 0.02 steps, $0.75, 0.82$ and 1.

Initial x-ray measurements of the PLCMO deposited on STO revealed a chemical phase-separation of the films into an LCMO and a PCMO phase. To ensure thorough mixing of the ablated material on the substrate, a 10 s pause was inserted between each 30 pulse cycle. XRD patterns of films grown in the second manner show that the PLCMO now consists of a single chemical phase (figure 5.1).

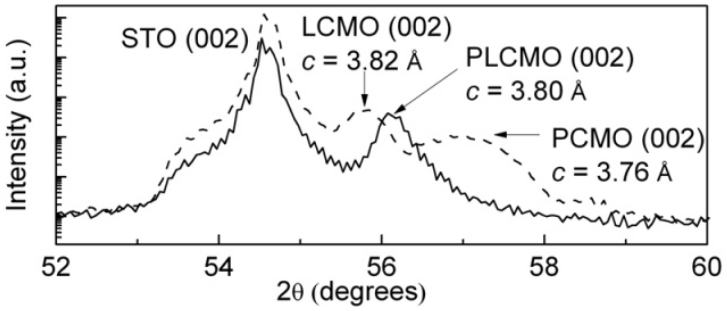

Figure 5.1: Crystal quality of films grown on STO substrates with and without waiting time. The films deposited without waiting time (dotted line) show a chemical phase-separation.

5.2 Microstructure and stoichiometry

The single-phase nature, orientation and lattice structure of the as-grown films have been characterised by $\theta - 2\theta$ x-ray diffraction and reciprocal space mapping around the (013) reflection. X-ray diffraction measurements give evidence that the 100 nm thick PLCMO films consist of a single chemical phase and are epitaxially oriented in a cube-on-cube way on the substrate. For the films grown on STO, the diffraction patterns show a gradual increase of the c lattice parameter from 3.78 Å to 3.83 Å with increasing La content (figure 5.2). The increase in lattice parameter is an effect of the increasing lattice parameters from PCMO to LCMO and is consistent with the presence of tensile strain in the films induced by the larger lattice parameter of the STO substrate. On PMN-PT, the films grow with widely different lattice parameters ranging from 3.82 Å to 3.86 Å for a nominally equal composition of $y = 0.6$ (figure 5.3). This is attributed to the large lattice mismatch of substrate and film[1], and the variation in miscut (up to 2°) and roughness of the as-received PMN-PT substrates. Reciprocal space mapping around the (013) peak shows that the films grow nearly coherently on the STO substrates (figure 5.4). The films on PMN-PT are in a residual tensile strain state which is tetragonally distorted with $c/a < 1$ (figure 5.5). The lattice parameters of the end members of the series, as well as of selected films on STO and PMN-PT, can be found in table 5.1.

Atomic force microscopy (AFM) has been employed to investigate the surfaces of the films. AFM images reveal rather smooth film surfaces grown in an island-type manner, with a rms roughness $\sigma < 1$ nm for all films. The roughness on PMN-PT has been evaluated within one ferroelectric domain of the substrate, i.e. in a typical area of 1 x 2 μm^2.

[1]The pseudotetragonal in-plane lattice parameter of poled PMN-PT substrates is $a = b = 4.022$Å [1, 2], which is $4 - 5\%$ larger than the pseudocubic lattice parameters of the end members of the film series, PCMO ($a = 3.806$ Å) and LCMO ($a = 3.864$ Å). On STO ($a = 3.905$ Å), the lattice mismatch is $1 - 3\%$.

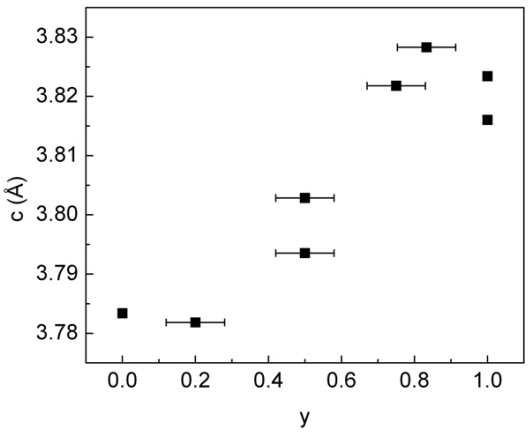

Figure 5.2: c-lattice parameter of PLCMO on STO v. La content y. The error bars are derived from the averaged error in composition measured by XPS.

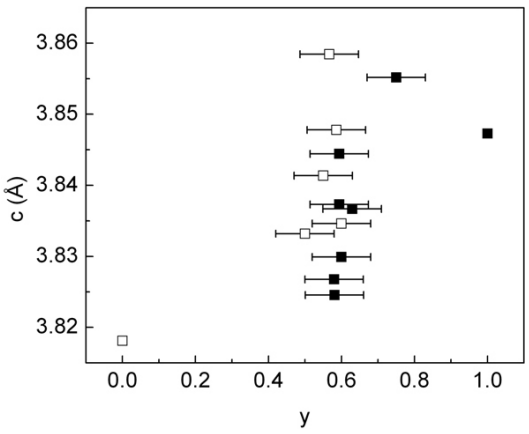

Figure 5.3: c-lattice parameter of PLCMO on PMN-PT v. La content y. The open and closed symbols indicate samples with an insulating and a metallic ground state, respectively.

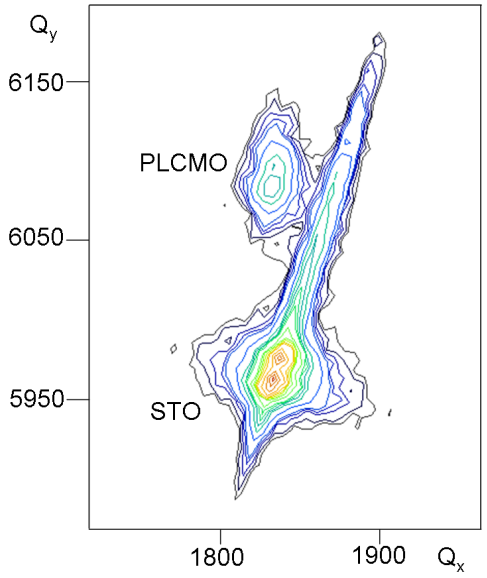

Figure 5.4: Reciprocal space map around the (013) reflection of a PLCMO film with $y = 0.75$ showing coherent growth of the film on STO.

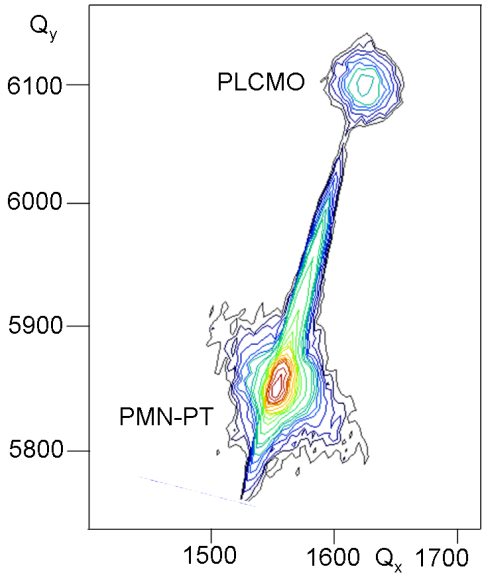

Figure 5.5: Reciprocal space map around the (013) reflection of a PLCMO film with $y = 0.6$ on PMN-PT, showing a residual strain state which is tetragonally distorted with $c/a < 1$.

Substrate	y	a lattice parameter (Å)	c lattice parameter (Å)	c/a
STO	0	3.908	3.792	0.970
STO	0.5	3.899	3.806	0.976
STO	0.75	3.898	3.827	0.982
STO	1	3.901	3.819	0.979
PMN-PT	0	3.84	3.81	0.992
PMN-PT	0.6	3.88	3.84	0.990
PMN-PT	1	3.87	3.85	0.995

Table 5.1: Lattice parameters of the end members of the $(Pr_{1-y}La_y)_{0.7}Ca_{0.3}MnO_3$ series as well as of selected other compositions. The a and c parameters have been recorded by reciprocal space mapping.

The compositions of the films have been analysed by x-ray photoelectron spectroscopy (XPS)[2]. In figure 5.6, the XPS results are compared to the nominal composition of films grown on PMN-PT for a range of y values around the metal-insulator phase boundary. The individual data points represent concentration values from several film depths. The agreement between the nominal y calculated from the ratio of the laser pulses on the PCMO and LCMO targets and the averaged value derived from the XPS measurements is within 8%. The XPS depth profiles (figure 5.7) show no concentration gradients with depth, giving evidence of a good mixing of

[2]XPS measurement done by Dr. S. Oswald

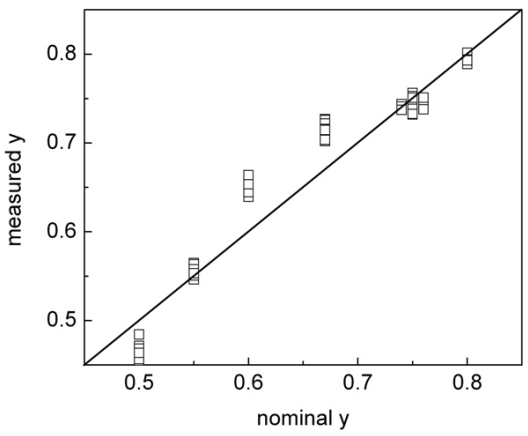

Figure 5.6: Composition y measured by XPS plotted versus the nominal y calculated from the number of laser pulses.

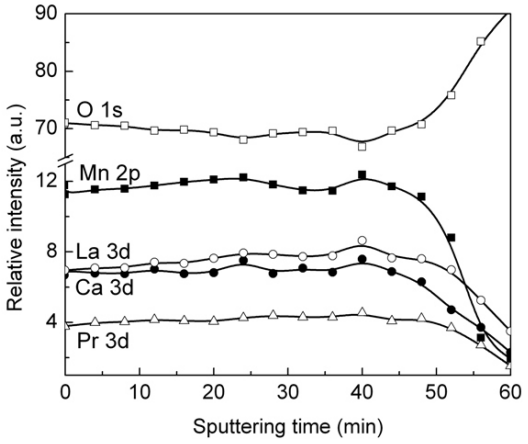

Figure 5.7: XPS depth profile for a film with $y = 0.63$ on PMN-PT. The relative intensity of the various elements is plotted v. the sputtering time.

the components throughout the volume of the film. These observations indicate a successful control of the Pr/La ratio of the films by the applied alternating ablation method from two targets.

5.3 Physical properties in dependence on composition

Resistivity measurements in dependence on temperature and magnetic field have been carried out on the PLCMO films in four-probe geometry in a cryostat equipped with a superconducting magnet and a cryogen-free refrigerator cryostat. A sufficiently low measuring current I ≤ 10 μA was chosen so that the films showed Ohmic behaviour and no field- or current-induced conductivity variations.

Figure 5.8 shows the temperature dependence of the resistance of several films on PMN-PT with y varied around the metal-insulator phase boundary. Thermal hysteresis is shown for the film with $y = 0.59$. In agreement with earlier studies of both bulk and thin film samples, a gradual change from the insulating to the metallic ground state is observed with increasing La content, and the metal-insulator transition temperature T_{MI} increases with y. A sample is referred to as "insulating" if the resistance is above the measurable range at 10 K. This is done for practical reasons and does not strictly mean the absence of a resistance peak at low temperatures. For compositions below $y = 0.60 \pm 0.05$ the films are insulating at low temperatures. Close to $y = 0.6$, both metallic and insulating samples have been found. Therefore, the composition $y = 0.60 \pm 0.05$ represents the metal-insulator phase boundary of the PLCMO films on PMN-PT. The variation in the behaviour of films with $y = 0.6$ is attributed to the uncertainty in the composition, in combination with the varied strain states of the as-grown films on PMN-PT.

Magnetic measurements show a systematic increase of the Curie temperature with increasing La content (figures 5.9 and 5.10). In particular, a steep rise of T_C can be seen around the metal-insulator boundary at $y = 0.6$. The correlation between the rise in T_C and the MI boundary has been noted earlier in bulk studies [3, 4, 5]. The T_C of the LCMO end member is suppressed with respect to the bulk value by 50 K on PMN-PT and by 70 K on STO. This suppression is essentially attributed to the tensile strain in the films [6]. The T_C of the other end member, PCMO, is reduced by 20 K and 25 K with respect to the bulk value on PMN-PT and STO, respectively. Apart from the specific composition at the metal-insulator phase boundary, these observations are in line with the known phase diagram of PLCMO (figure 2.5) [4, 5, 7, 8].

At the metal-insulator transition, percolating electron transport takes place through the FMM clusters embedded in the COI antiferromagnetic matrix. The low-temperature high-field magnetisation M(10 K, 5 T) of the films with $y \leq 0.6$ is reduced to values below 200 emu/cm^3, which is in line with the idea that only a fraction of the film volume is ferromagnetic. (For ferromagnetically aligned Mn spins, an ideal magnetisation of 640 emu/cm^3 is expected.) A distinct transition to a long-range CO state has not been observed in the electrical transport data of the films with y

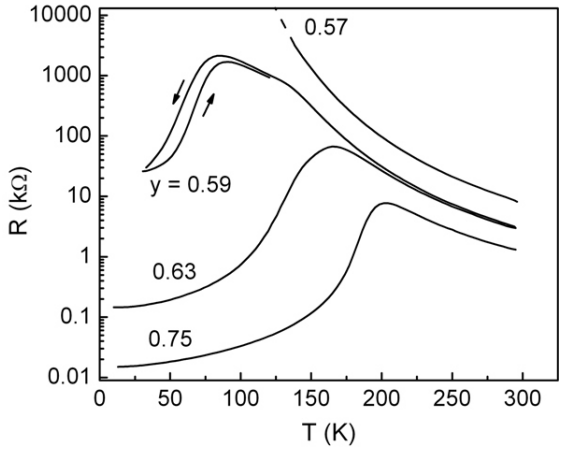

Figure 5.8: Electrical resistance of PLCMO films on PMN-PT as a function of temperature for various values of y. Thermal hysteresis is shown for $y = 0.59$.

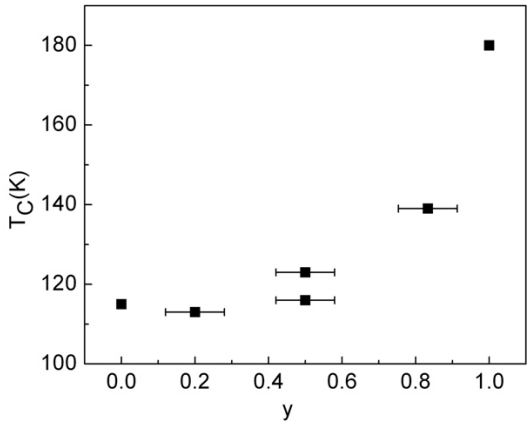

Figure 5.9: Curie temperature as a function of y for films grown on STO.

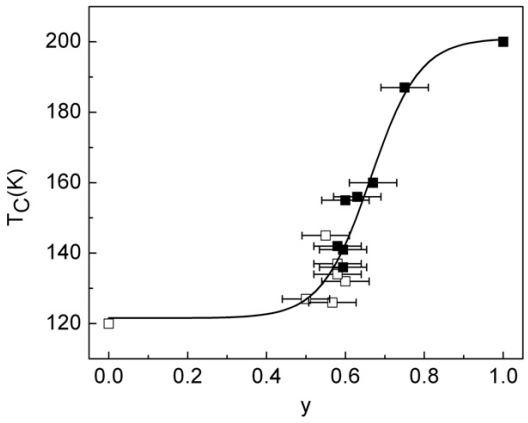

Figure 5.10: T_C in dependence on composition y. Open and closed symbols indicate samples with insulating and metallic ground states, respectively.

≤ 0.6, and no distinct antiferromagnetic transition is found in their temperature-dependent magnetisation data at any temperature. This is, however, not unusual for strained films with compositions where the CO state is not very pronounced. Other typical features attributed to the phase coexistence in earlier studies, such as the strong hysteresis in temperature and magnetic field dependent resistance data, have been registered (figure 5.8).

5.4 Influence of reversible substrate strain

To carry out strain-dependent measurements of the films grown on PMN-PT, a voltage V $\leq$ 200 V was applied along the substrate normal between the PLCMO film on top and a NiCr/Au electrode on the bottom (001) face of the substrate, producing an electric field of $E \leq 6.7$ kV/cm in the 0.3 mm thick substrate. The substrate shrinks approximately linearly with increasing E in both in-plane directions. The maximum field of 6.7 kV/cm leads to 0.07 % $\pm$0.01 compression between 300 K and 90 K [1, 6].

In PLCMO films with $y \approx 0.6$, resistive and magnetic measurements suggest a strong competition between the ferromagnetic metallic and charge ordered insulating ground states. Therefore, the effect of strain on the balance between the phases is expected to be largest in this region, and the study of the reversible strain will be focussed on these films.

5.4.1 Resistance

The electrical resistance of the films depends sensitively on the substrate-induced strain. Figure 5.11 shows a substrate field cycle between +6.7 kV/cm and −6.7 kV/cm for a $y = 0.6$ film. An approximately linear in-plane expansion occurs for negative field values as long as the ferroelectric coercive field of the substrate is not yet reached [9]. The resistance of the film decreases under biaxial compression ($E > 0$), and increases under expansion ($E < 0$). It tracks the reversible in-plane substrate strain in an approximately proportional way, but in more detail, the curve is non-linear and hysteretic. Since the strain v. field characteristic of the substrate is not in itself hysteretic as long as the polarisation is not switched [6], the measured hysteresis originates from the response of the PLCMO film to the substrate strain. The hysteresis may be another manifestation of the phase-separated nature of the films, where the phase boundaries move irreversibly during strain changes. The resistance is not affected by the electric field itself, since that effect should be independent of the sign of E, which is contrary to the observations in figure 5.11.

Most strain-dependent measurements have been done in a unipolar manner (not switching the substrate polarisation) to limit the probability of fracture of the PMN-PT. Figure 5.11 also shows a unipolar strain measurement at 104 K for a $y = 0.6$ sample. The elastoresistance of the film in figure 5.11 is $[R(0)-R(6.7\text{kV/cm})]/R(0) = 64$ % for the measurement shown in the upper right panel. The resistive gauge factor Γ

is defined as the elastoresistance divided by the applied strain. For the film in figure 5.11, $\Gamma = 914$ for the full strain range. For smaller magnitudes of E, values of Γ up to 1800 may be observed (figure 5.11, lower right panel). A value of $\Gamma \approx 1800$ is extraordinarily large for a bulk effect. Recently, a giant room-temperature piezoresistance with $\Gamma = 843$ has been observed for an aluminium-silicon hybrid [10], and strained Si nanowires show gauge factors around $\Gamma = 1000$ [11]. Strain-dependent resistance measurements have been taken at various temperatures for films with $y = 0.6$ and a metallic (figure 5.12) or an insulating (figure 5.13) ground state. The largest elastoresistance is observed in metallic films with $y \approx 0.6$ at temperatures close to the metal-insulator transition temperature. Derived resistive gauge factors are as high as $\Gamma \approx 1000$. Even larger values would be possible depending on the steepness of the $R(T)$ characteristics at T_{MI}. Due to the magnitude of the effect and a temperature dependence similar to the colossal magnetoresistance effect in manganites, the term "colossal" elastoresistance has been suggested [12]. The elastoresistance observed in the insulating films is much smaller (figure 5.13), with a gradual increase of the gauge factor upon lowering the temperature. Again, a qualitative similarity in the temperature dependence of the elastoresistance and the magnetoresistance is evident, here for the insulating films. The applied piezo-compression was not sufficient to turn an insulating film metallic in the ground state. Contrary to what is known for the magnetoresistance, the elastoresistance does not vanish above the Curie temperature. At 300 K, far above the Curie temperature of the $y = 0.6$ samples, still Γ values near 25 are recorded. The elastic deformation of the unit cell also affects

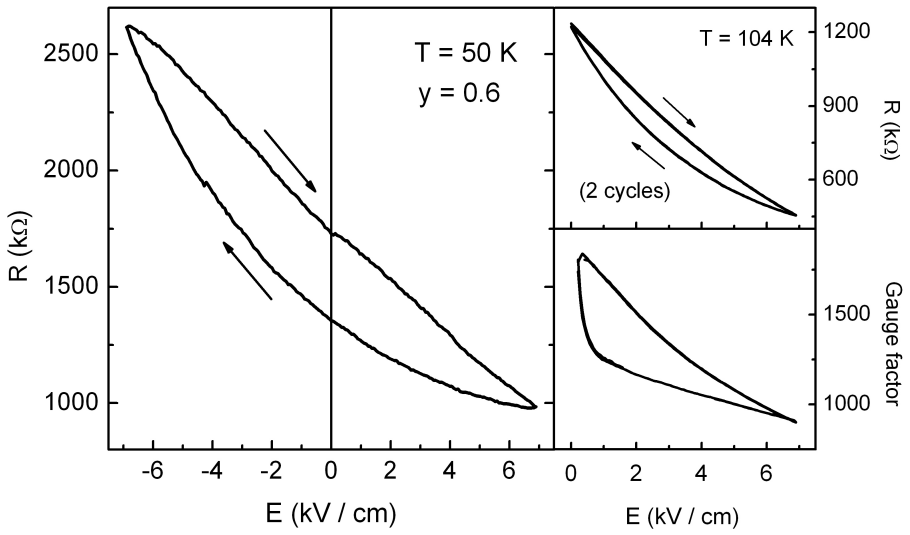

Figure 5.11: Left panel: Resistance of a $y = 0.6$ sample as a function of the electric field applied to control the substrate strain. Positive fields result in an in-plane compression, negative fields in an expansion of the films. Right panels: Strain dependent resistance measurement at 104 K for a $y = 0.6$ sample (top) with the corresponding gauge factor (bottom).

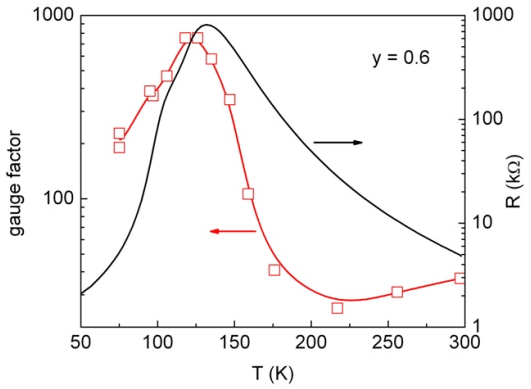

Figure 5.12: Gauge factor and resistance v. temperature for a metallic sample with $y = 0.6$.

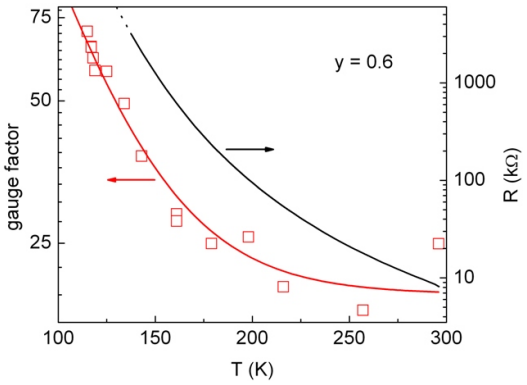

Figure 5.13: Gauge factor and resistance v. temperature for an insulating film with $y = 0.6$.

the high temperature electrical transport, whereas the field-induced magnetic order becomes negligibly weak far above T_C.

Summarising, we find a substantial reduction of the resistance when the as-grown tensile strain of the film is partially released by piezo-compression of the substrate. This effect is seen in all investigated films, regardless of the composition or the electronic nature of the ground state. In other words, all films show a positive elastoresistance, and the release of tensile strain acts qualitatively similar to an applied magnetic field, enhancing the electrical conductivity.

5.4.2 Magnetisation

In the following part, the effect of the reversible substrate strain on the magnetisation of the PLCMO films is described. Figure 5.14 represents a typical measurement of a field-dependent $M(H)$ loop in the as-grown and the piezo-strained state of a $y = 0.6$ film. Consistent with the transport results, the piezoelectric release of tensile strain leads to an increase in the magnetisation associated with the decrease in the resistance. The magnetic coercive field remains the same for the applied magnitude of strain, indicating a weak effect of the reversible strain on the magnetocrystalline anisotropy. In contrast, the high-field magnetisation is enhanced by more than 10% for the data taken near T_C.

Figure 5.15 shows $M(T)$ for the as-grown and the piezo-compressed state of a $y = 0.6$ film with a metallic ground state. In prototypical ferromagnetic manganites, such as $La_{0.7}Sr_{0.3}MnO_3$, a strain-dependent T_C underlies the strain-dependent spontaneous (or saturation) magnetisation measured at constant temperatures [13]. In PLCMO, however, only a certain fraction of the film is ferromagnetic in the ground state. Therefore, in contrast to a typical ferromagnet with a collinear FM ground state, where a shift of T_C is expected to have negligible influence far below T_C, the magnetisation of PLCMO may show a strain response not only close to T_C,

but also at lower temperatures.

The effect of a strain-dependent shift of T_C on the magnetisation can be estimated from the change in M as follows: The $M(T)$ data of the as-grown strain state are shifted with respect to the T axis by ΔT_C, the T_C shift under the piezo-strain, and the difference $\Delta M^*/M(0)$ between both data sets is calculated. ΔT_C is then adjusted so that $\Delta M^*/M(0)$ fits best to the measured $\Delta M/M(0)$ around T_C [9]. The result of this approximation, will overestimate the real effect of a T_C shift for temperatures $T << T_C$. From the $M(T)$ data in figure 5.15, a T_C shift of 2 K has been estimated for the PLCMO film, leading to a value of $dT_C/d\epsilon = 28$ K/%. Similar values have been found for other films with $y \approx 0.6$.

Comparing the measured $\Delta M/M(0)$ to the fit, the actual change in M is more than twice as large as the expected value at temperatures T < 100 K. This low temperature behaviour differs from the behaviour of prototypical ferromagnetic manganites and demonstrates an additional effect of strain on the low-temperature magnetic order. The different temperature dependence of the strain-induced change in the magnetisation is also visible in figure 5.16, where the $\Delta M/M(0)$ of several PLCMO films is compared to that of a typical ferromagnetic $La_{0.7}Sr_{0.3}MnO_3$ film. The prototypical FM film shows a more pronounced peak around T_C than the PLCMO film. On the other hand, the PLCMO films display a more gradual decay of the effects of strain towards low temperature. The latter may be understood as an effect of the reversible strain on the phase-separated magnetic state of the PLCMO films. The low-temperature strain response of the magnetisation in particular reaches a maximum for the $y \approx 0.6$ samples at the metal-insulator phase boundary.

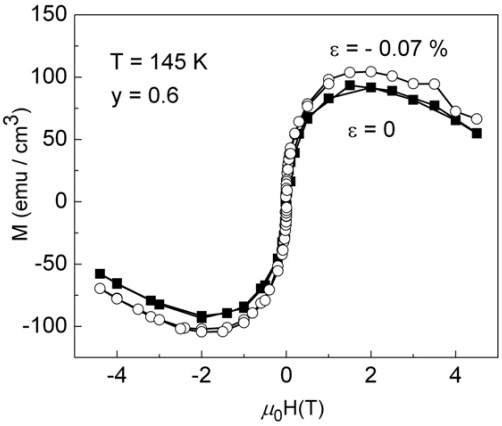

Figure 5.14: Magnetisation loop v. applied magnetic field of a sample with $y = 0.6$ in the as-grown strained state ($\epsilon = 0$) and after piezo-compression of the substrate.

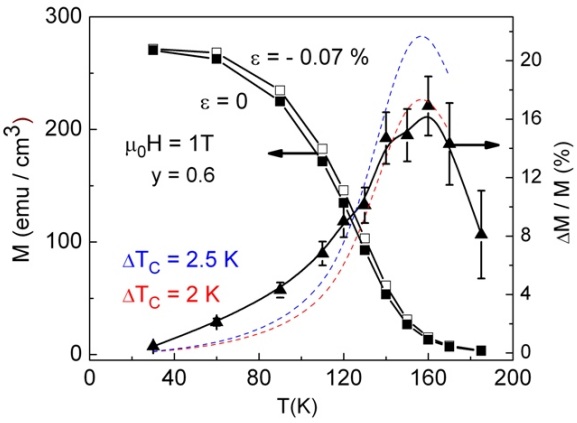

Figure 5.15: Magnetisation v. temperature of a film with $y = 0.6$ in two strain states. The change in M (closed triangles) is fitted by a strain induced shift in T_C of 2 K (red line) and 2.5 K (blue line).

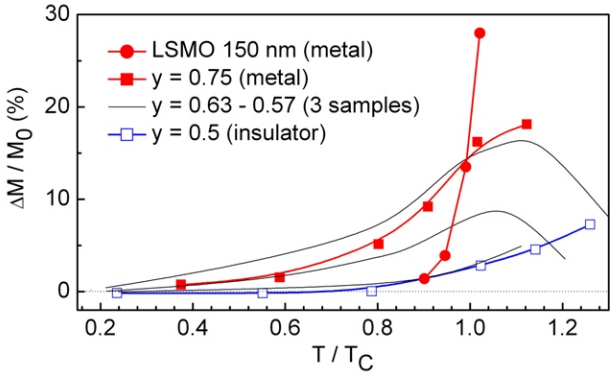

Figure 5.16: Temperature dependence (normalised to T_C) of the strain induced change in the magnetisation of several PLCMO films compared to that of a typical $La_{0.7}Sr_{0.3}MnO_3$ film.

The results of the magnetisation and resistance measurements performed in controlled strain states demonstrate a strong suppression of the ferromagnetic double exchange by tensile strain. The piezoelectric release of the tensile strain leads to a significant increase of the magnetisation and a huge reduction in the resistance. The release of tensile strain reduces the tetragonal distortions in PLCMO. This brings the O−Mn−O bond angles closer to 180°, aligning the Mn spins and increasing electron hopping. Additionally, the competing CO-AFM state might be strengthened by the tensile strain, since the latter might stabilise the in-plane e_g orbitals. A more detailed mechanism of the effect of strain on the phase-separated FMM/CO-AFM state, such as a change in volume fraction of the two phases, is difficult to deduce from the investigation of macroscopic properties. It may be speculated that the maximum elastoresistance near the metal-insulator transition is related to the percolative nature of the transport mechanism, with the release of strain leading to enlarged metallic regions in the sample. In contrast, the smaller strain response of the insulating films seems to reflect the effect of strain on the insulating matrix around FMM clusters.

5.5 Conclusions

In order to investigate the effect of reversible biaxial substrate strain on the properties of the phase-separated PLCMO system, films have been prepared with a range of compositions $y = 0 - 1$ on STO and on piezoelectric PMN-PT substrates. The metal-insulator phase boundary has been established to lie at $y \approx 0.6$. Measurements of the magnetisation prove a systematic increase of T_C with increasing La content. In particular, a steep rise of T_C can be seen around $y = 0.6$.

By application of an electric field of $E \leq 6.7$ kV/cm along the substrate normal, the in-plane lattice parameter of the PMN-PT substrate is reversibly compressed.

The resulting release of tensile strain in the film plane induces a drastic reduction of the resistance, or a colossal elastoresistance, in films with $y \approx 0.6$. Gauge factors as high as $\Gamma = 1000$ have been found around the metal-insulator transition temperature, which is an extraordinarily large value for a bulk effect. The elastoresistance is highest at the chemical composition $y \approx 0.6$ (the metal-insulator phase boundary) and near the metal-insulator transition temperature, where the competition between the FM and CO ground states is strongest. This indicates that the coexistence of the FM and CO phases is strongly affected by reversible substrate strain.

Consistent with the transport results, the piezoelectric release of tensile strain leads to an increase in both the ferromagnetic transition temperature and the magnetisation. Compared to prototypical FM manganites, the PLCMO system shows a much more gradual decay of the strain induced change in the magnetisation towards low temperatures. This is likely to be an effect of the strain response of the mixed-phase state. Both the magnetisation and the resistance data reveal a strong suppression of the ferromagnetic double exchange interaction by tensile strain in the films.

Bibliography

[1] *Reversible uniform strain in epitaxial oxide films*, M.D. Biegalski, K. Dörr, D.-H. Kim, H.M. Christen, unpublished

[2] *In-situ X-ray investigation of a $PbMg_{1/3}Nb_{2/3}O_3$-28%$PbTiO_3$ single-crystal plate in an external electric field*, A.A. Levin, D.C. Meyer, P. Paufler, C. Thiele, K. Dörr, L. Schultz, Appl. Phys. A: Mater. Sci. Process. **84**, 37 (2006)

[3] *Percolative phase separation underlies colossal magnetoresistance in mixed-valent manganites*, M. Uehara, S. Mori, C.H. Chen, S.-W. Cheong, Nature (London) **399**, 560 (1999)

[4] *Competition between coexisting phases in (La,Pr)$CaMnO_3$ manganites*, S.H. Masunaga, R.F. Jardim, J. Appl. Phys. **102**, 073903 (2007)

[5] *Comparative study of the magnetic phase diagrams of $(La_{1-y}Pr_y)_{0.7}Ca_{0.3}MnO_3$ with oxygen isotopes ^{16}O and ^{18}O*, A.M. Balagurov, V.Y. Pomjakushin, D.V. Sheptyakov, N.A. Babushkina, O.Y. Gorbenko, A.R. Kaul, Physica B (Amsterdam) **350**, 1 (2004)

[6] *Influence of strain on the magnetization and magnetoelectric effect in $La_{0.7}A_{0.3}MnO_3$/PMN-PT (001) (A=Sr,Ca)*, C. Thiele, K. Dörr, O. Bilani, J. Rödel, L. Schultz, Phys. Rev. B **75**, 054408 (2007)

[7] *Current oscillation and low-field colossal magnetoresistance effect in phase-separated manganites*, M. Tokunaga, H. Song, T. Tokunaga, T. Tamegai, Phys. Rev. Lett. **95**, 157203 (2005)

[8] *Imaging of Percolative Conduction Paths and Their Breakdown in Phase-Separated $(La_{1-y}Pr_y)_{0.7}Ca_{0.3}MnO_3$ with y=0.7*, M. Tokunaga, Y. Togunaga, T. Tamegai, Phys. Rev. Lett. **93**, 037203 (2004)

[9] *Reversible strain effect on the magnetization of $LaCoO_3$ films*, A. Herklotz, A.D. Rata, L. Schultz, K. Dörr, Phys. Rev. B **79**, 092409 (2009)

[10] *Giant Room-Temperature Piezoresistance in a Metal-Silicon Hybrid Structure*, A.C.H. Rowe, A. Donoso-Barrera, Ch. Renner, S. Arscott, Phys. Rev. Lett. **100**, 145501 (2008)

[11] *Giant piezoresistance effect in silicon nanowires*, R. He, P. Yang, Nat. Nanotechnol. **1**, 42 (2006)

[12] *Colossal elastoresistance and strain-dependent magnetization of phase-separated* $(Pr_{1-y}La_y)_{0.7}Ca_{0.3}MnO_3$ *thin films*, M.C. Dekker, A.D. Rata, K. Boldyreva, S. Oswald, L. Schultz, and K. Dörr, Phys. Rev. B **80**, 144402 (2009)

[13] *Quantifying strain dependence in "colossal" magnetoresistance manganites*, A.J. Millis, T. Darling, A. Migliori, J. Appl. Phys. **83**, 1588 (1998)

Chapter 6

$[La_{0.7}Sr_{0.3}MnO_3/SrTiO_3]$ superlattices

$La_{0.7}Sr_{0.3}MnO_3$ (LSMO) thin films have properties that vary from those of the bulk material. In particular, substrate induced lattice strain causes structural modifications which strongly affect the magnetic properties of the films [1]. In this chapter, the magnetic behaviour of superlattices (SL) of $La_{0.7}Sr_{0.3}MnO_3$ and $SrTiO_3$ is described. The quality of superlattices grown on STO and PMN-PT substrates is compared. In particular, the effect of reversible substrate strain on the magnetic properties in dependence on the thickness of the LSMO layers is discussed. The second part of the chapter deals with the transfer of the reversible strain through the layers of the superlattice.

6.1 Growth

The $[LSMO/STO]_{d/k}$[1] superlattices were grown by off-axis pulsed laser deposition from stoichiometric targets of $La_{0.7}Sr_{0.3}MnO_3$ and $SrTiO_3$. The samples were grown simultaneously on monocrystalline PMN-PT substrates and on conventional STO substrates in order to compare the superlattice quality. The films were deposited at an oxygen pressure of $p = 0.3$ mbar, at a substrate temperature of T = 700°C and with a pulse frequency of $f = 3$ Hz, resulting in a growth rate of 0.2 Å per pulse. Superlattices were grown with a LSMO thickness ranging from 1.9 nm (5 unit cells) to 16.7 nm (43 unit cells) on PMN-PT. In each sample, $d = d_{\mathrm{LSMO}} = d_{\mathrm{STO}}$. The deposition always started with the LSMO layer.

To compare the crystal quality, a $[LSMO/STO]_{6.7nm/23}$ superlattice has been prepared by RHEED assisted pulsed laser deposition[2]. The superlattice has been grown on a TiO_2 terminated $SrTiO_3$ substrate, at an oxygen pressure of $p = 0.3$ mbar at a substrate temperature of T = 650°C and with a pulse frequency of $f = 3$ Hz, resulting in a growth rate of 0.05 Å per pulse. The deposition of this superlattice started with the STO layer.

[1] For clarity, we will refer to the superlattices (SL) as $[LSMO/STO]_{d/k}$, where d is the thickness of the individual layers of the SL and k is the number of LSMO/STO bi-layers in the system. It is assumed that $d = d_{LSMO} = d_{STO}$.

[2] Sample deposited by Andreas Herklotz, Oak Ridge National Laboratory.

6.2 XRD measurements

The single-phase nature, orientation and lattice structure of the as-grown films have been characterised by $\theta - 2\theta$ x-ray diffraction, reciprocal space mapping around the (013) reflection and x-ray reflectivity measurements. The $\theta - 2\theta$ scans of superlattices with different d (figure 6.1) show $(00h)$ reflections only, indicating that the superlattices are epitaxially oriented in a cube-on-cube way on the substrate. Satellite peaks can be seen up to the 4th order on both STO and PMN-PT. The position of the 0th order peak is independent of both the superlattice period and the total thickness of the sample up to at least 234 nm, indicating that there is no relaxation of the substrate induced tensile strain throughout the layers. On STO, since the 0th order peak of the superlattice overlaps with the peak of the substrate, the position of the 0th order peak is taken to be the average of the two 1st order peaks. The superlattice period Λ has been calculated from the position of the satellite peaks. The thickness of the LSMO layer is taken to be half the superlattice period $d = \Lambda/2$.

Reciprocal space mapping around the (013) reflection shows that the superlattices on STO grow coherently on the substrate (figure 6.2). The in-plane and out-of-plane lattice parameters are independent of d and k and have been recorded as $a = 3.905$ Å and $c = 3.906$ Å. On PMN-PT, the superlattices show a residual tensile strain state which is tetragonally distorted with $c/a < 1$ (figure 6.2). The lattice parameters on PMN-PT are $a = 3.912$ Å and $c = 3.901$. Taking the pseudocubic bulk lattice constants of STO (3.905 Å) and LSMO (3.876 Å), this corresponds to a residual in-

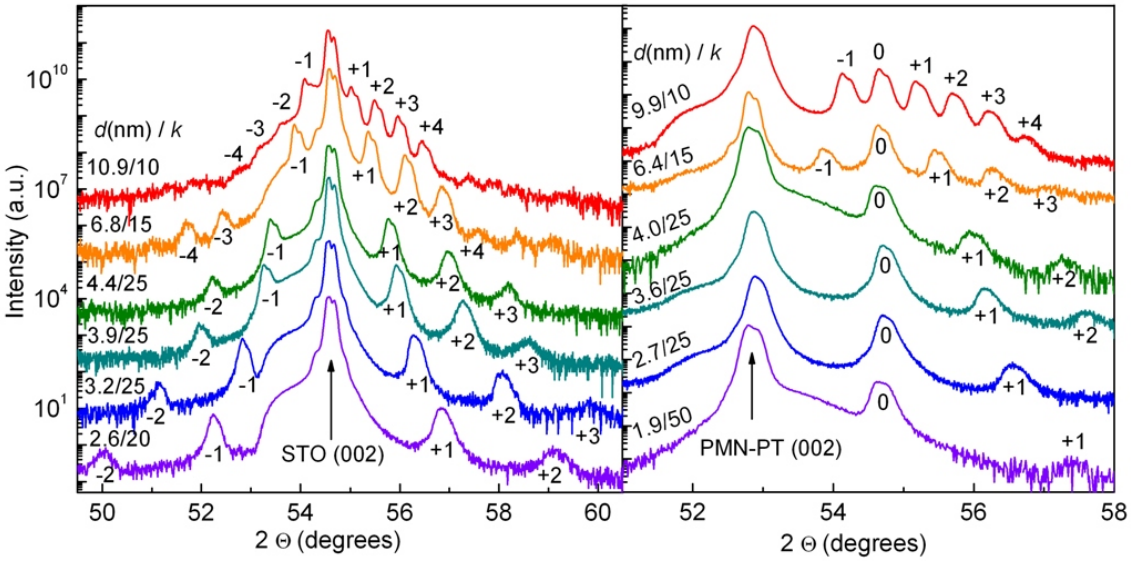

Figure 6.1: $\theta - 2\theta$ XRD scans around the (002) reflection of [LSMO/STO] superlattices grown on STO (left panel) and PMN-PT (right panel). d denotes the thickness of the LSMO layer, k the number of bilayers in the system. The scans are vertically displaced for clarity.

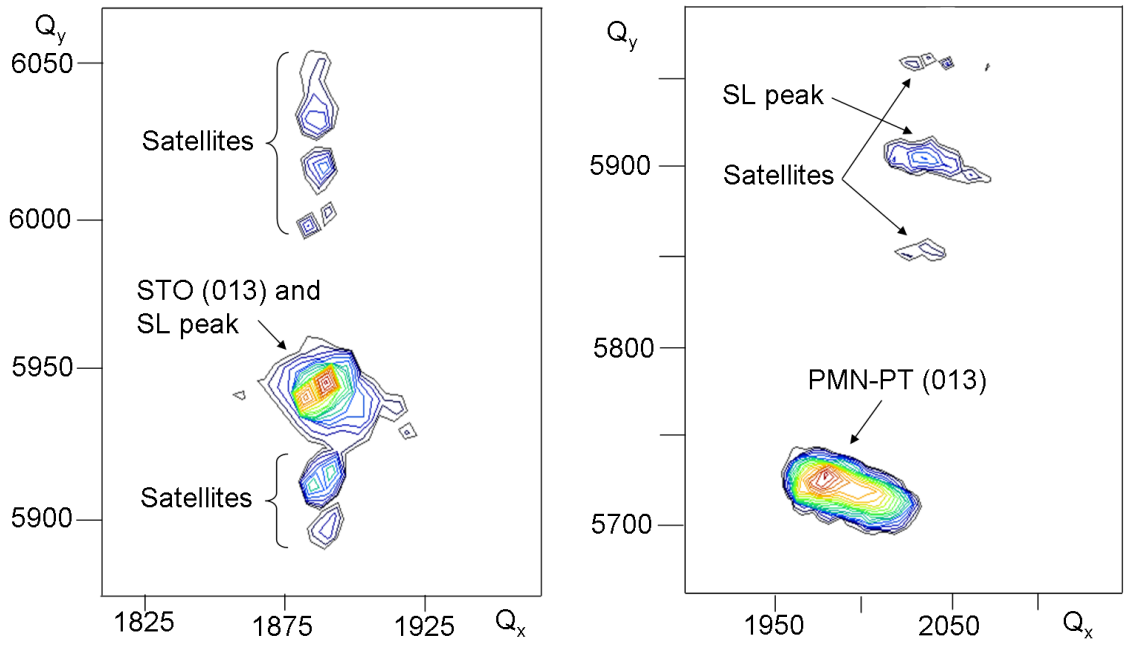

Figure 6.2: Left panel: Reciprocal space map around the (013) reflection of a $[\mathrm{LSMO/STO}]_{6.8nm/15}$ SL on STO. The superlattice grows fully strained on the substrate. Right panel: RSM around the (013) reflection of a $[\mathrm{LSMO/STO}]_{2.7nm/25}$ SL on PMN-PT. The SL has a residual tensile strain state in which the LSMO is tetragonally distorted with $c/a < 1$.

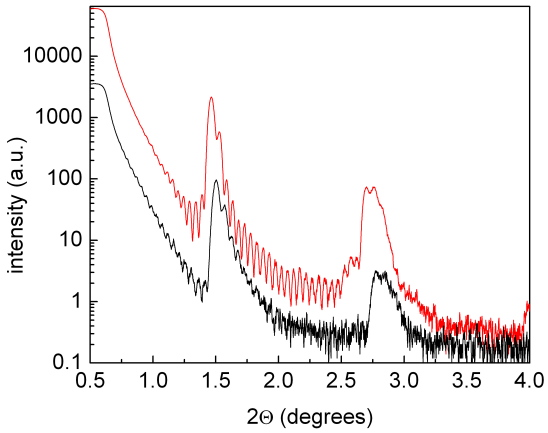

Figure 6.3: XRR measurements of a $[\mathrm{LSMO/STO}]_{3.2nm/25}$ superlattice on STO (red curve) and a $[\mathrm{LSMO/STO}]_{2.7nm/25}$ SL on PMN-PT (black curve).

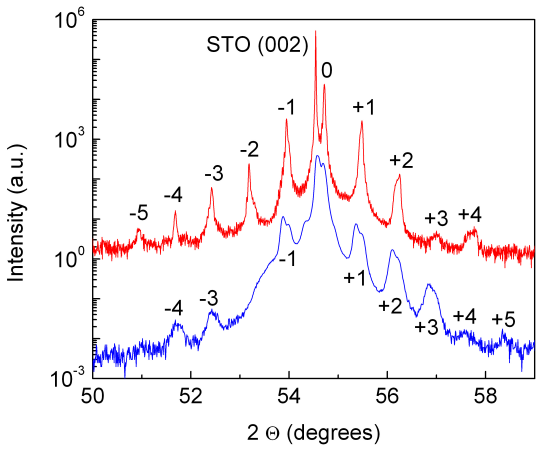

Figure 6.4: XRD measurements of a SL with $d = 6.7$ nm, grown by RHEED assisted PLD (red curve) and a SL with $k = 15$, $d = 6.8$ nm, grown by conventional PLD (blue curve). The scans are vertically displaced for clarity.

plane tensile strain of 0.7 % (LSMO) and 0 % (STO) for the superlattices grown on STO substrates and 0.9 % (LSMO) and 0.2 % (STO) on PMN-PT.

X-ray reflectivity measurements (figure 6.3) show clear Kiessig oscillations as well as the larger interference maxima caused by the superlattice peaks, giving qualitative proof of a well defined superlattice structure with sharp interfaces on both the STO and the PMN-PT substrates.

XRD patterns of two superlattices on STO deposited with and without the assistance of RHEED are shown in figure 6.4. The superlattices have a comparable LSMO thickness of $d = 6.7$ nm and $d = 6.8$ nm, with $k = 23$ and $k = 15$ for the RHEED and non-RHEED sample, respectively. The samples show a comparable number of superlattice reflections, indicating a comparable crystal quality. (The superlattice peaks of the RHEED-sample appear sharper due to the XRD measurement being done with a Ge-monochromator, filtering out the Cu Kα_2 radiation. The non-RHEED sample is measured with Co Kα_1 and Kα_2 radiation, making the peaks appear more broad.) The out-of-plane lattice parameter of the RHEED-sample is $c = 3.893$ Å, slightly smaller than that of the non-RHEED sample ($c = 3.906$ Å), suggesting that the RHEED-sample has a larger in-plane tensile strain.

Due to the roughness of the PMN-PT substrates, it is not possible to see RHEED intensity oscillations on PMN-PT. Trials have been made to deposit a superlattice in parallel on STO and PMN-PT substrates, counting the intensity oscillations on the STO. However, XRD measurements of the superlattice on PMN-PT show additional phases, and the overall superlattice quality of the non-RHEED samples is higher on PMN-PT.

6.3 Magnetisation

Magnetisation measurements in dependence on temperature and magnetic field have been carried out in a superconducting quantum interference device (Quantum Design, 5 T). All samples show a ferromagnetic transition at T_C which decreases from 338 K for $d = 16.7$ nm to 56 K for $d = 1.9$ nm on PMN-PT (figure 6.5). The steep drop in T_C seen for $d < 5$ nm is reflected in a decrease of the saturation magnetisation M_{sat} and an increase of the coercive field H_c (figure 6.6). In general, the superlattices grown on PMN-PT show a more gradual decrease of M_sat, and the coercive fields are higher than in the samples grown on STO for all d. A drop in T_C, combined with an increase in H_c and a decrease in M_{sat}, has been noted before [2, 3, 4] and has been ascribed to the finite size effect.

6.4 The effect of reversible substrate strain

To carry out the strain-dependent magnetisation measurements, a voltage $V \leq 300$ V was applied along the normal of the PMN-PT substrates, producing an electric field of $E \leq 10$ kV/cm between the superlattice on top and a NiCr/Au electrode on the bottom (001) of the 0.3 mm thick substrate. The applied electric field corre-

sponds to an in-plane compression of the substrate of 0.11 % ± 0.01 between 300 K and 90 K [5].

A typical measurement of the temperature dependent magnetisation in the as-grown and piezo-strained state is shown in figure 6.7. The release of tensile substrate strain leads to an increase in the magnetisation at all temperatures. The relative change in magnetisation between the two strain states $\Delta M/M_0$ increases towards higher temperature and reaches a maximum slightly above T_C. The sample in figure 6.7, $[\mathrm{LSMO/STO}]_{2.7nm/25}$, shows a shift in T_C per strain of about 66 K / %.

Figure 6.8 shows the relative change in magnetisation $\Delta M/M_0$ in dependence on the normalised temperature T/T_C of five superlattices with different d. In all superlattices, $\Delta M/M_0$ is highest slightly above T_C and decreases when the temperature is lowered. For the superlattices with the thickest LSMO layers, $\Delta M/M_0$ shows a steep decrease of the strain response below T_C. This behaviour is comparable to that of single, thick layers of LSMO, where a strain-dependent T_C underlies the strain-dependent spontaneous (or saturation) magnetisation [1]. The shift in T_C per strain of the superlattice with $d = 16.7$ nm is estimated to be $dT_C/\epsilon_{xx} = 64$ K / %. A comparison of the strain response of this superlattice with a 150 nm thick single film of LSMO is shown in figure 6.9. As expected in ferromagnets with a collinear FM ground state, the shift of the Curie temperature has a negligible influence far below T_C, and $\Delta M/M_0$ vanishes quickly for $T < 0.9\ T/T_C$.

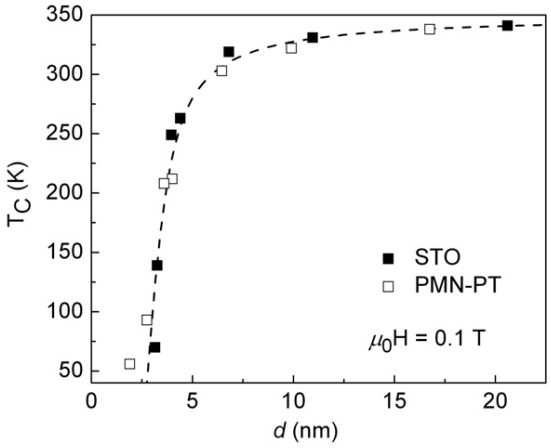

Figure 6.5: Magnetic transition temperature as a function of d for the superlattices grown on STO (closed squares) and PMN-PT (open squares). (The dotted line is a guide to the eye.)

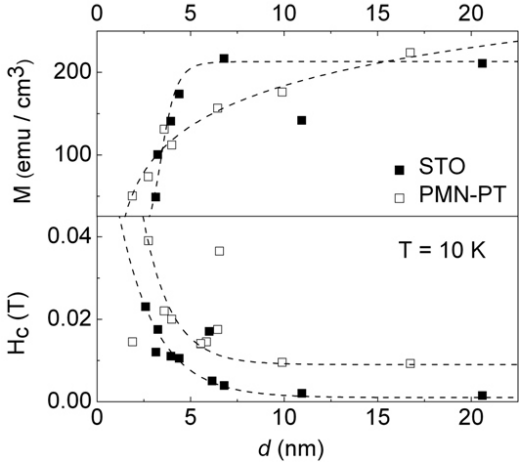

Figure 6.6: Saturation magnetisation (upper panel) and coercive field (lower panel) in dependence on the LSMO layer thickness. (The dotted lines are guides to the eye.)

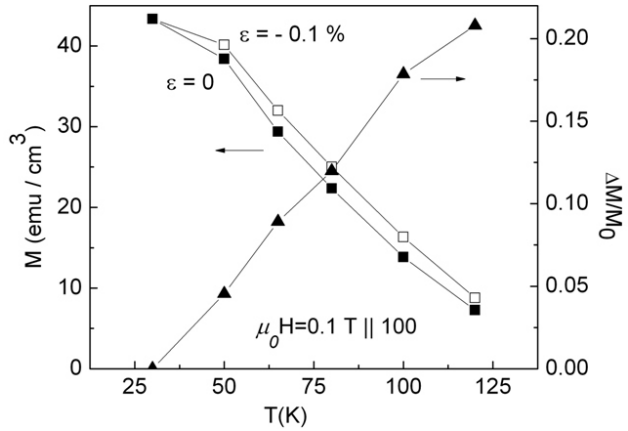

Figure 6.7: A typical measurement of the magnetisation in the as-grown (closed squares) and piezo-strained (open squares) state as well as the relative change in the magnetisation $\Delta M/M_0$ (closed triangles) plotted v. temperature. The thickness of the LSMO layers is 2.7 nm, and $k = 25$.

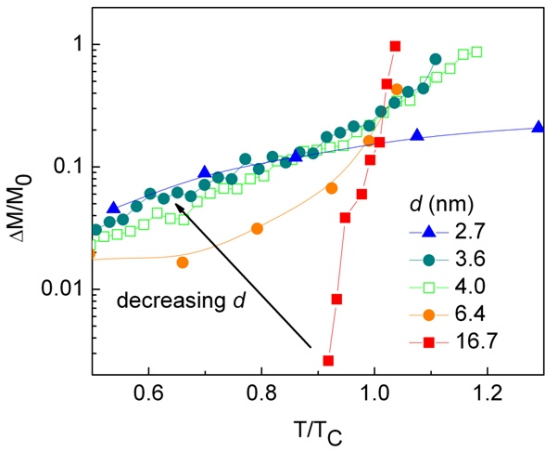

Figure 6.8: Strain induced change in magnetisation $\Delta M/M_0$ in dependence on the normalised temperature T/T_C of five superlattices with different LSMO layer thickness.

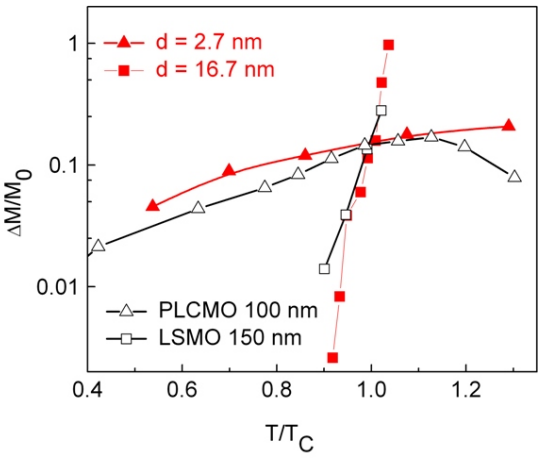

Figure 6.9: Temperature dependence of the strain induced change in M of two SLs with $[\mathrm{LSMO/STO}]_{2.7nm/25}$ and $[\mathrm{LSMO/STO}]_{16.7nm/5}$, compared to single thick films of PLCMO (100 nm) and LSMO (150 nm).

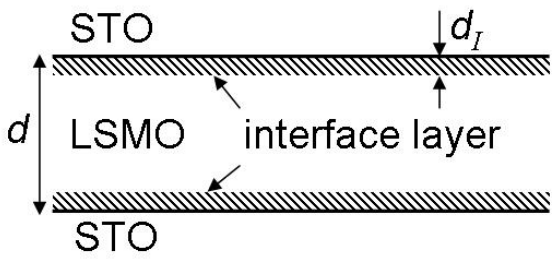

Figure 6.10: Schematic drawing of the LSMO/STO interface, showing the phase-separated magnetically "dead" interface layer.

When the thickness of the LSMO layers in the superlattice is decreased from $d = 16.7$ nm to $d = 2.7$ nm, the strain response of the magnetisation at low T increases: samples with $d < 4$ nm still show a change in M of several percent at $T \leq 0.5\ T/T_C$. This low-temperature behaviour cannot be explained by assuming a ferromagnetic state with a strain-dependent T_C only. A comparable low-temperature response has been found in single films of $(Pr_{1-y}La_y)_{0.7}Ca_{0.3}MnO_3$ (PLCMO), where it has been attributed to the phase-separated nature of the material (see 5.4.2) [6]. In figure 6.9, the strain response of the magnetisation of a superlattice with $d = 2.7$ nm is compared to the response of a 100 nm thick single film of PLCMO. In the phase-separated PLCMO, the substrate induced strain has been suggested to influence the magnetic phase coexistence, with the release of tensile strain favouring the FM metallic state [6].

Ultra-thin films of LSMO display a modified magnetic behaviour compared to thicker films [7, 8, 9, 10]. This finding led to the proposal of the existence of an interface layer which is insulating as well as magnetically disordered over the whole temperature range. As the origin of this so-called magnetically "dead" layer, a mixed phase state, with nanoscale electronically separated ferromagnetic metallic and charge/orbital ordered insulating clusters has been suggested [11, 12]. In the superlattices, the increase of $\Delta M/M_0$ with decreasing d at low temperature may be explained within the picture of the LSMO interface layer showing phase-separated tendencies (figure 6.10). As d is decreased, the relative volume fraction of the interface layer increases and the low temperature behaviour of the superlattice changes from that of a conventional ferromagnet to that of a phase-separated system.

Within the picture of a phase-separated layer at the LSMO interface, it may be possible to derive a value for the thickness d_I of this layer from measurements of the absolute change in the magnetisation per interface. Two different phenomena contribute to the strain induced change in magnetisation: one is the shift of the magnetic transition temperature caused by the "bulk" part of the LSMO layers upon the release of the tensile substrate strain, the other is the effect of strain on the phase-separated state of the interface. Since the effect of the "bulk" part is negligibly small below $T < 0.9\ T_C$, it may be assumed that any effect below $T = 0.9\ T_C$ is essentially

caused by changes in the magnetisation of the interface layer. In a simplified picture, the "bulk" part of the LSMO layers gets smaller as d is decreased and it disappears completely when $d = 2d_I$. Note that this will not change the strain response of M at temperatures $T < 0.9\ T_C$. A further decrease of d, however, should be visible as a decrease of the absolute change of the magnetisation per interface. Figure 6.11 shows the change in magnetic moment Δm per interface for five superlattices with $d = 1.9 - 6.4$ nm. The superlattices with 6.4 nm $> d >$ 3.6 nm show a comparable Δm per interface. For $d \leq 2.7$ nm, however, Δm gets progressively smaller. This puts the thickness of the layer showing no "bulk" effects between 3.6 nm and 2.7 nm. Since each LSMO layer has two interfaces with STO, a value for the thickness of the phase-separated, magnetically "dead" interface layer may be derived of 13.5 Å $< d_I <$ 17 Å on PMN-PT.

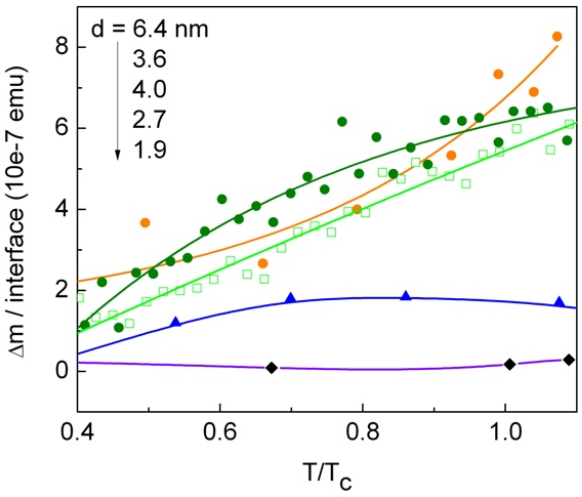

Figure 6.11: Change in the magnetic moment per interface of five superlattices with d between 1.9 and 6.4 nm.

6.5 Strain transfer through the interfaces

In this part of the chapter, the question of the transfer of the reversible substrate strain through the layers of a superlattice is addressed. From earlier measurements on single films grown on PMN-PT, it is known that the strain is transferred through films of a thickness up to at least 200 nm [13]. However, it has to be checked if the many different layers present in superlattices influence the strain transfer, e.g. by lattice defects at the interfaces between the different compounds.

6.5.1 X-ray measurements in different strain states

The in-plane lattice parameters of the PMN-PT substrates can be controlled by the application of an external electric field. A sufficiently large field will effectively

pole the substrate, changing the crystal lattice structure from rhombohedral to monoclinic M_A [14, 15]. In the monoclinic state, the ferroelectric polarisation is directed along the body diagonal of the pseudocubic cell, and the substrates poled along the 001 direction contain four different domain variants with a stable domain configuration [16]. Since the monoclinic state has a different lattice parameter than the rhombohedral state, poling and un-poling the PMN-PT substrates creates the opportunity to investigate samples in two different static strain states [17]. In order to pole the substrates, a voltage of $V = 300$ V has been applied to the PMN-PT for 15 minutes. To un-pole the substrates, the PMN-PT has been heated for 20 min at 200 °C, which is above the ferroelectric transition temperature of 140 °C.

X-ray $\theta - 2\theta$ measurements in the Bragg-Brentano configuration give c lattice parameters averaged over seven different PMN-PT substrates in the un-poled and the poled state of $c = 4.026$ Å and $c = 4.023$ Å, respectively. The full width at half maximum (FWHM) of the substrate (002) peaks changes from 0.217° in the un-poled state to 0.167° in the poled state.

In order to investigate the transfer of the substrate strain through the layers of a superlattice, XRD measurements have been performed on the LSMO/STO superlattices in the poled and the un-poled state of the substrate. The c lattice parameters of the SL are on average 0.002 Å smaller in the un-poled state. The FWHM of the 0th order superlattice peaks is 0.238° in the un-poled and 0.239° in the poled state. If the strain transfer through the layers of the superlattice would be less than complete, poling of the substrate would result in an inhomogeneous in-plane strain of the sample. The larger variation in the c lattice parameter due to the changing of the strain throughout the layers would be seen as a broadening of the FWHM of the 0th order peak as compared to the un-poled state. The FWHM of the samples in both strain states remains the same within the error of measurement. This indicates that the reversible substrate strain is transferred fully through all the interfaces of the superlattice. However, since the strain difference between the poled and the un-poled state is very small, this is a preliminary result.

To better quantify the change in the lattice parameter of the superlattices, XRD measurements using the reversible strain method have been performed in a four-circle diffractometer[3]. Figure 6.12 shows the (004), (200) and (220) reflections of the PMN-PT substrate and a superlattice with $d = 2.7$ nm in the poled state (no applied electric field) and under an applied electric field of $E = 15$ kV/cm. Upon release of the tensile strain, both the superlattice and the substrate show an increase in the c lattice parameter and a decrease in the a lattice parameter. The measured values for a and c, as well as the shifts in lattice parameter da and dc, are listed in table 6.1. The in-plane shift of the lattice parameters between the poled and the piezo-strained state is the same for the superlattice and the PMN-PT substrate within the error of measurement, giving further evidence that the reversible strain is fully transferred through the layers.

[3]XRD measurement done by Andreas Herklotz at Oak Ridge National Laboratory.

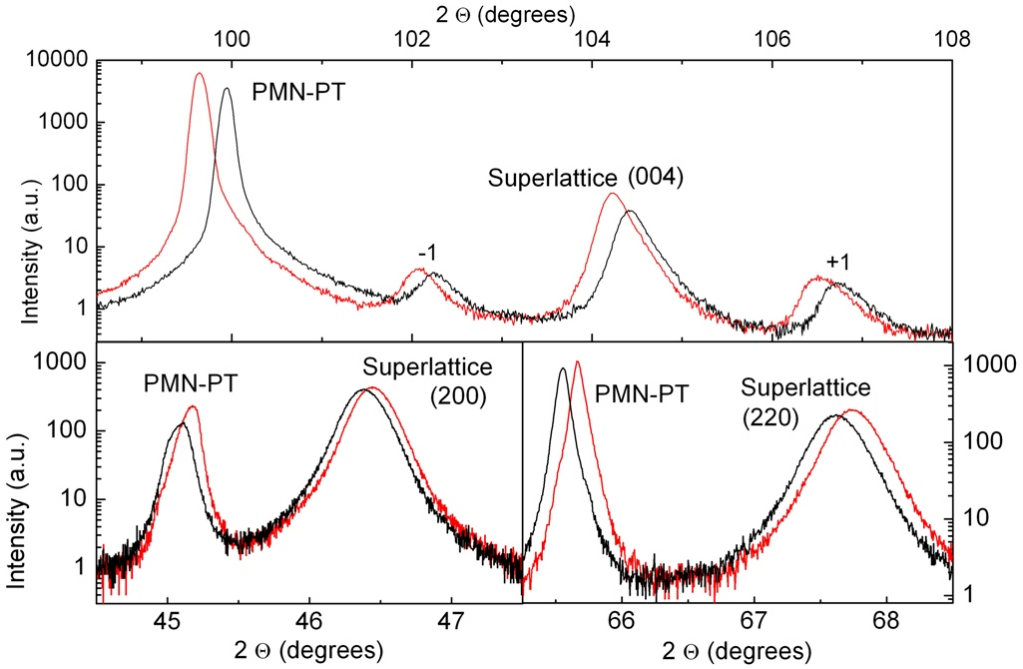

Figure 6.12: XRD measurements of a superlattice with $d = 2.7$ nm in the poled (black curves) and piezo-strained (red curves) state. The applied electric field is $E = 15$ kV/cm.

	c (Å) ($E = 0$ kV/cm)	c (Å) ($E = 15$ kV/cm)	dc (Å)
Superlattice	3.899	3.904	0.005
PMN-PT	4.024	4.033	0.009
	a (Å) ($E = 0$ kV/cm)	a (Å) ($E = 15$ kV/cm)	da (Å)
Superlattice (200)	3.912	3.907	0.005
Superlattice (220)	3.916	3.909	0.007
PMN-PT (200)	4.017	4.011	0.006
PMN-PT (220)	4.024	4.018	0.006

Table 6.1: a and c lattice parameters of a superlattice with $d = 2.7$ nm and of the PMN-PT substrate in the strained and piezo-compressed state. The data are taken from the x-ray measurements in figure 6.12.

6.5.2 Magnetisation

When the tensile strain in the LSMO/STO superlattices is partially released by piezo-compression of the substrate, the change in the lattice parameter is reflected in an increase of the magnetisation. To investigate the transfer of the strain through the layers of the superlattice, superlattices with equal d, but different thickness have been prepared. Figure 6.13 shows the normalised magnetisation in dependence on temperature of three superlattices with $d = 5.5$ nm and a total thickness of 55.5 nm, 111 nm and 234 nm. The thinner superlattice shows a slightly lower magnetic transition temperature of $T_C = 315$ K, compared to 329 K and 331 K for the 234 nm and 111 nm samples. The c lattice parameters of the superlattices are $c = 3.858$ Å, $c = 3.866$ Å and $c = 3.868$ Å for the 55.5 nm, 111 nm and 234 nm superlattices, respectively. Therefore, the difference in T_C may be due to the higher as-grown strain state of the thinnest sample.

Comparing the relative change in magnetisation upon the release of tensile strain $\Delta M/M_0$ of the different SLs (figure 6.13), the 55.5 nm superlattice exhibits a slightly higher strain response than the 111 nm and 234 nm samples at all temperatures. Since the c lattice parameter in the as-grown state of the thinner superlattice lies farther away from the bulk value than in the other two samples, a higher strain response is to be expected. The 111 nm and 234 nm superlattices have a comparable c lattice parameter and T_C. Within the error of measurement, $\Delta M/M_0$ is equal in both superlattices, but due to the large error of measurement and the extreme sensitivity of $\Delta M/M_0$ on the as-grown strain state of the material, it is difficult to derive conclusive proof that the strain-transfer through the interfaces is complete.

To show that the reversible substrate strain can in principle be transferred through many layers, a 50 nm thick layer of LSMO has been prepared on top of a superlattice consisting of 50 bi-layers of LSMO/STO. Magnetisation measurements on this sample (figure 6.14) reveal two clear magnetic transition temperatures. The T_C of the thick LSMO layer is 355 K, which is close to the value found in bulk samples (370 K). The superlattice has a T_C of about 100 K, which is comparable to the temperatures found for the superlattices in the first part of this chapter. Strain dependent magnetisation measurements (figure 6.15) reveal two peaks in $\Delta M/M_0$, the first resulting from the superlattice around $T = 70$ K and the second from the thick LSMO layer on top at $T = 355$ K. The relatively low value of $\Delta M/M_0$ of the superlattice results from the large magnetisation of the LSMO layer at low temperatures, which contributes to M_0, but not to ΔM. The maximum value of $\Delta M/M_0$ of the LSMO films is 12 % around T_C. For single thick LSMO films, the response of the magnetisation to strain lies between 10% and 20% around T_C, depending on the as-grown strain state of the film [18]. This experiment, therefore, gives, if not exact values, a proof of principle that the reversible substrate strain of the PMN-PT is transferred through at least 100 layers into the LSMO on top.

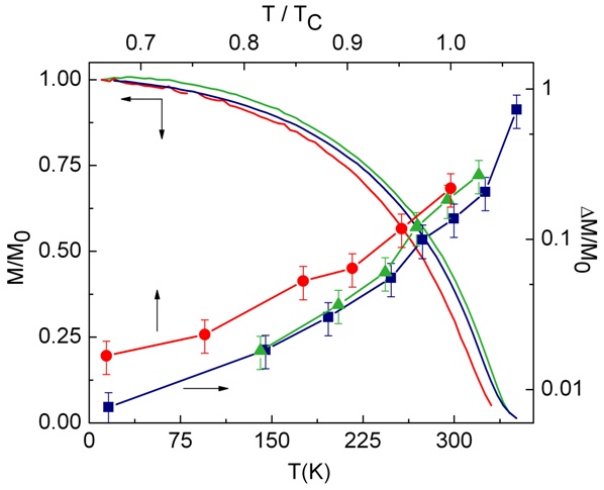

Figure 6.13: Normalised magnetisation v. temperature (left and bottom axes) of three SLs with $d = 5.5$ nm and a thickness of 55.5 nm (red), 111 nm (blue) and 234 nm (green). Also plotted is $\Delta M/M_0$ v. temperature normalised to T_C (right and top axes). The error has been estimated from several runs of strain measurements performed at the same temperature.

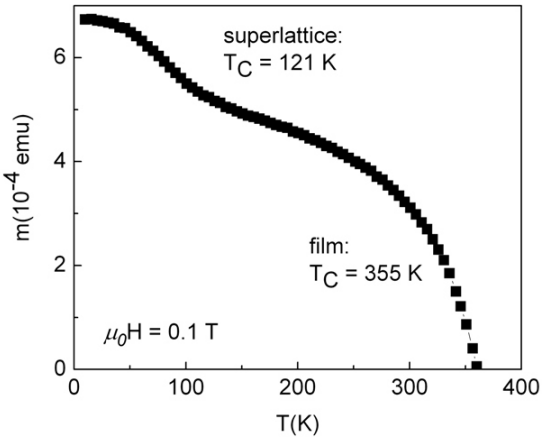

Figure 6.14: Temperature dependent magnetic moment of a 50 nm layer of LSMO on top of an LSMO/STO superlattice with $d = 2$ nm and 50 bilayer repetitions.

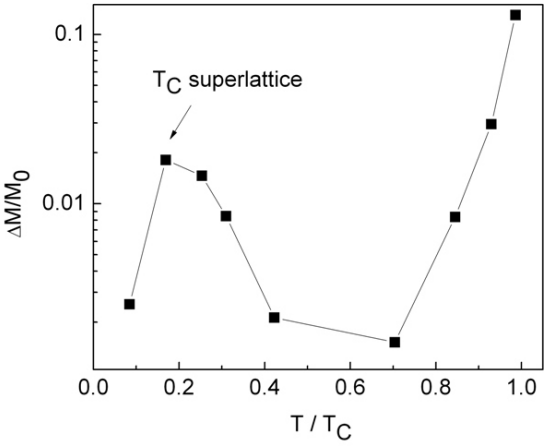

Figure 6.15: Relative strain induced change in the magnetisation of the SL of figure 6.14 v. temperature normalised to the T_C of the thick top LSMO layer.

6.6 Conclusions

[LSMO/STO] superlattices have been deposited by pulsed laser deposition on STO and piezo-electric PMN-PT substrates. XRD measurements reveal comparable crystal quality of the superlattices grown on STO and PMN-PT. XRR measurements show clear Kiessig fringes as well as the larger interference maxima caused by the superlattice peaks, giving qualitative proof of a well defined superlattice structure with sharp interfaces on both substrates. In more detail, the XRR measurements reveal a slightly higher roughness of the superlattices grown on PMN-PT. With decreasing LSMO layer thickness d, the samples show a sharp decrease of the Curie temperature, accompanied by a decrease of the saturation magnetisation and an increase of the coercive field around $d = 5$ nm. Reversible strain measurements on thicker superlattices ($d = 16.7$ nm) reveal a behaviour of the magnetisation similar to that of single thick films of LSMO. When d is decreased, the strain induced relative change in magnetisation $\Delta M/M_0$ shows a behaviour comparable to PLCMO thin films. This has been attributed to the increased volume fraction of the LSMO interface layer with STO, which displays a reduced magnetic order and phase-separated tendencies. From the absolute change in magnetisation per interface, the thickness of the so-called magnetically "dead" layer of the LSMO has been estimated to lie between 13.5 Å and 17 Å in the superlattices grown on PMN-PT.

XRD measurements of the superlattices on PMN-PT in the poled and un-poled state of the substrate show no variation in the FWHM of the superlattice peaks, indicating a complete transfer of the reversible substrate strain through the layers of the superlattice. More detailed measurements of the a and c lattice parameters in the poled (no applied field) and the piezo-strained state reveal equal changes of the in-plane lattice parameters of the substrate and the superlattice. Magnetic measurements on superlattices with equal d but a different total thickness show no change in $\Delta M/M_0$ within the error of measurement. However, the sensitivity of $\Delta M/M_0$ on the as-grown strain state of the material makes quantitative conclusions with regard to the amount of strain transferred through the superlattice layers difficult. In a further experiment, the strain response of a thick layer of LSMO deposited on a superlattice consisting of 50 bi-layers of LSMO/STO has been found to be comparable to that of a single thick film of LSMO grown directly on PMN-PT. Together, these experiments may serve as a proof of principle that the reversible substrate strain is transferred through at least 100 layers of a superlattice.

Bibliography

[1] *Quantifying strain dependence in "colossal" magnetoresistance manganites*, A.J. Millis, T. Darling, A. Migliori, J. Appl. Phys. **83**, 1588 (1998)

[2] *Magnetotransport of $La_{0.7}Sr_{0.3}MnO_3/SrTiO_3$ multilayers with ultrathin manganite layers*, K. Dörr, T. Walter, M. Sahana, K.-H. Müller, K. Nenkov, K. Brand, L. Schultz, J. Appl. Phys. **89**, 6973 (2001)

[3] *Magnetic properties of heteroepitaxial $La_{0.7}Sr_{0.3}MnO_3/SrTiO_3$ superlattices*, M. Sahana, T. Walter, K. Dörr, K.-H. Müller, D. Eckert, K. Brand, J. Appl. Phys. **89** 6834 (2001)

[4] *Magnetoresistance of heteroepitaxial $La_{0.7}Sr_{0.3}MnO_3/SrTiO_3$ multilayers*, T. Walter, K.-H. Müller, K. Dörr, M. Sahana, K. Nenkov, K. Brand, L. Schultz, Sensors and Actuators A **91**, 184 (2001)

[5] *$SrTiO_3$ on piezoelectric PMN-PT(001) for application of variable strain*, O. Bilani-Zeneli, A.D. Rata, A. Herklotz, O. Mieth, L.M. Eng, L. Schultz, M.D. Biegalski, H.M. Christen, K. Dörr, J. Appl. Phys. **104**, 054108 (2008)

[6] *Colossal elastoresistance and strain-dependent magnetization of phase-separated $(Pr_{1-y}La_y)_{0.7}Ca_{0.3}MnO_3$ thin films*, M.C. Dekker, A.D. Rata, K. Boldyreva, S. Oswald, L. Schultz, K. Dörr, Phys. Rev. B **80**, 144402 (2009)

[7] *Thickness-dependent magnetotransport in ultrathin manganite films*, J.Z. Sun, D.W. Abraham, R.A. Rao, C.B. Eom, Appl. Phys. Lett. **74**, 3017 (1999)

[8] *Suppression of the metal-insulator transition temperature in thin $La_{0.7}Sr_{0.3}MnO_3$ films*, M. Angeloni, G. Balestrino, N.G. Boggio, P.G. Medaglia, P. Orgiani, A. Tebano, J. Appl. Phys. **96**, 6387 (2004)

[9] *Magnetic and electric "dead" layers in $La_{0.7}Sr_{0.3}MnO_3$ thin films*, R.P. Borges, W. Guichard, J.G. Lunney, J.M.D. Coey, F. Ott, J. Appl. Phys. **89**, 3868 (2001)

[10] *Critical thickness and orbital ordering in ultrathin $La_{0.7}Sr_{0.3}MnO_3$ films*, M. Huijben, L.W. Martin, Y.-H. Chu, M.B. Holcomb, P. Yu, G. Rijnders, D.H.A. Blank, R. Ramesh, Phys. Rev. B **78**, 094413 (2008)

[11] *Electronic phase separation in manganite-insulator interfaces*, L. Brey, Phys. Rev. B **75**, 104423 (2007)

[12] *Charge trapping in optimally doped epitaxial manganite thin films*, M. Bibes, S. Valencia, L. Balcells, B. Martínez, J. Fontcuberta, M. Wojcik, S. Nadolski, E. Jedryka, Phys. Rev. B **66**, 134416 (2002)

[13] *Reversible uniform strain in epitaxial oxide films*, M.D. Biegalski, K. Dörr, D.-H. Kim, H.M. Christen, unpublished

[14] *Phase diagram of the ferroelectric relaxor* $(1-x)PbMn_{1/3}Nb_{2/3}O_3 - xPbTiO_3$, B. Noheda, D.E. Cox, G. Shirane, J. Gao, Z.-G. Ye, Phys. Rev. B **66**, 054104 (2002)

[15] *Electric-field-, temperature-, and stress-induced phase transitions in relaxor ferroelectric single crystals*, M. Davis, D. Damjanovic, and N. Setter, Phys. Rev. B **73**, 014115 (2006)

[16] *Ultrahigh strain and piezoelectric behavior in relaxor based ferroelectric single crystals*, S.E. Park, T.R. Shrout, J. Appl. Phys. **82**, 1804 (1997)

[17] *Investigation of substrate-induced strain effects in* $La_{0.7}Ca_{0.15}Sr_{0.15}MnO_3$ *thin films using ferroelectric polarization and the converse piezoelectric effect*, R.K. Zheng, Y. Jiang, Y. Wang, H.L.W. Chan, C.L. Choy, H.S. Luo, Appl. Phys. Lett. **93**, 102904 (2008)

[18] *Influence of strain on the magnetization and magnetoelectric effect in* $La_{0.7}A_{0.3}MnO_3$*/PMN-PT (001) (A=Sr,Ca)*, C. Thiele, K. Dörr, O. Bilani, J. Rödel, and L. Schultz, Phys. Rev. B **75**, 054408 (2007)

Chapter 7

Summary and outlook

This work describes the effect of reversible elastic lattice strain on the phase-separated electronic ground state of a) thin films of $(Pr_{1-y}La_y)_{0.7}Ca_{0.3}MnO_3$ (PLCMO) and b) the interface layer of $La_{0.7}Sr_{0.3}MnO_3$ (LSMO) with $SrTiO_3$ (STO).

In order to investigate the effect of reversible biaxial substrate strain on the properties of the phase-separated PLCMO system, films have been prepared with a La content ranging from $y = 0$ to $y = 1$ on both STO and piezoelectric PMN-PT substrates. XPS measurements show that the mixed ablation from a $La_{0.7}Ca_{0.3}MnO_3$ (LCMO) and a $Pr_{0.7}Ca_{0.3}MnO_3$ (PCMO) target produces chemically single phase films, and that the La/Pr ratio can be successfully controlled within 8 %. The metal-insulator phase boundary has been established to lie at $y = 0.6 \pm 0.05$. Measurements of the magnetisation reveal a systematic increase of T_C with increasing La content. In particular, a steep rise of T_C can be seen around $y = 0.6$.

By application of an electric field along the substrate normal, the lattice parameter of the PMN-PT substrate is reversibly compressed in both in-plane directions. The resulting release of tensile strain in the film plane induces a drastic reduction of the resistance, or a colossal elastoresistance, in films with $y = 0.6$. Resistive gauge factors as high as $\Gamma = 1000$ have been found around the metal-insulator transition temperature. The elastoresistance is highest at a chemical composition of $y = 0.6$ (the metal-insulator phase boundary), and near the metal-insulator transition temperature, where the competition between the FM and CO ground states is strongest.

Consistent with the transport results, the piezoelectric release of tensile strain leads to an increase in both the ferromagnetic transition temperature and the magnetisation. Compared to prototypical FM manganites, the PLCMO system shows a much more gradual decay of the strain response of the magnetisation towards low temperatures. This is attributed to the effect of the strain on the phase coexistence. Both the magnetisation and the resistance data in controlled strain states demonstrate a strong suppression of the ferromagnetic double exchange interaction by tensile strain in the films.

The [LSMO/STO] superlattices have been deposited on STO and on piezoelectric PMN-PT substrates by pulsed laser deposition. XRD measurements reveal a rather comparable crystal quality of the superlattices grown on STO and PMN-PT. XRR measurements show clear Kiessig fringes as well as the larger interference maxima

caused by the superlattice, giving qualitative proof of a well defined superlattice structure with sharp interfaces on both substrates. In more detail, the XRR measurements reveal a slightly higher roughness of the superlattices grown on PMN-PT. With decreasing LSMO layer thickness d, the samples show a sharp decrease of the Curie temperature, accompanied by a decrease of the saturation magnetisation and an increase of the coercive field around $d = 5$ nm. Reversible strain measurements on thicker superlattices ($d = 16.7$ nm) reveal a behaviour of the magnetisation similar to that of single thick films of LSMO. When d is decreased, the strain induced relative change in magnetisation $\Delta M/M_0$ shows a behaviour comparable to PLCMO thin films. This has been attributed to the increased volume fraction of the LSMO interface layer with STO, which displays a reduced magnetic order and phase-separated tendencies. From the absolute change in magnetisation per interface, the thickness of the so-called magnetically "dead" layer has been estimated to lie between 13.5 Å and 17 Å in the superlattices grown on PMN-PT.

XRD measurements of the superlattices on PMN-PT in the poled and the unpoled state of the substrate show no variation in the FWHM of the superlattice peaks, indicating a complete transfer of the reversible substrate strain through the layers of the superlattice. More detailed measurements of the a and c lattice parameters in the poled (no applied field) and the piezo-strained state reveal equal changes of the in-plane lattice parameters of the substrate and the superlattice. Magnetic measurements on superlattices with equal d but a different total thickness (110 nm and 230 nm) show no difference in $\Delta M/M_0$ within the error of measurement. However, the sensitivity of $\Delta M/M_0$ on the as-grown strain state of the material makes quantitative conclusions with regard to the amount of strain transferred through the superlattice layers difficult. Further measurements have been conducted on a thick layer of LSMO deposited on a superlattice consisting of 50 bilayers of LSMO/STO. The strain response of the thick LSMO layer is comparable to that of single thick layers of LSMO grown directly on PMN-PT. Together, these experiments may serve as a proof of principle that the reversible substrate strain is transferred through at least 100 layers of a superlattice.

In order to more precisely control the growth of manganites on piezo-electric PMN-PT substrates, in future work it may be attempted to prepare an improved PMN-PT surface so that the growth of the films can be monitored by RHEED. Since Pb is a very volatile element, annealing of the PMN-PT at high temperatures (> 800°C) might change the stoichiometry, and thus the strain response, of the substrate. The evaporation of Pb may be avoided by capping the substrate with a sufficiently thick buffer layer of e.g. STO, which may then be prepared for deposition in the manner of normal STO substrates. A slight interdiffusion of Pb into the STO buffer would not decrease the strain response of the bulk PMN-PT.

For the superlattices, refined XRD measurements are needed in order to evaluate the strain transfer through the layers in more detail. It should also be possible to create a superlattice with a thick layer of a different material on top. This way, the lattice parameter of the top layer will not overlap with that of the rest of the superlattice. This will make measurements of the change in lattice parameter of the

top layer more precise.

Where PLCMO is concerned, it would be interesting if the composition could be tuned more carefully to find the metal/insulator phase boundary. An insulating sample with a composition close enough to the phase boundary could then be turned metallic by the piezoelectric release of the tensile strain. This way, it would be possible to reversibly switch between a metallic and an insulating ground state.

Publications

1. *Colossal elastoresistance and strain-dependent magnetization of phase-separated* $(Pr_{1-y}La_y)_{0.7}Ca_{0.3}MnO_3$ *thin films*, M.C. Dekker, A.D. Rata, K. Boldyreva, S. Oswald, L. Schultz, K. Dörr, Phys. Rev. B **80**, 144402 (2009)

2. *A model system for strain effects: epitaxial magnetic films on a piezoelectric substrate*, K. Dörr, O. Bilani-Zeneli, A. Herklotz, A.D. Rata, K. Boldyreva, J.-W. Kim, M.C. Dekker, K. Nenkov, L. Schultz, M. Reibold, Eur. Phys. J. B **71**, 361 (2009)

3. *Large photoconductivity and light-induced recovery of the insulator-metal transition in ultrathin* $La_{0.7}Ce_{0.3}MnO_{3-\delta}$ *films*, E. Beyreuther, A. Thiessen, S. Grafström, L. M. Eng, M.C. Dekker, K. Dörr, Phys. Rev. B **80**, 075106 (2009)

4. *Reversibly strained* $[La_{0.7}Sr_{0.3}MnO_3/SrTiO_3]$ *superlattices; strain behavior of the magnetically "dead" layer*, M.C. Dekker, L. Schultz, K. Dörr, *submitted*

Acknowledgements

Herewith, I would like to express my thanks to all the people scientifically involved in the implementation of this thesis work at the IFW in Dresden. The IFW provides an international research environment and I would like to thank Prof. Ludwig Schultz for giving me the opportunity to work there.

My heartfelt gratitude goes to Dr. Kathrin Dörr, for her supervision of this work. Thank you, Kathrin, for your useful insights, open minded discussions and for showing me how to write proper scientific English.

Many thanks go to Dr. Diana Rata, for helping me to get to grips with the four-circle diffractometer. Diana, thank you for your valuable suggestions and help with the RSM and XRR measurements and your patience in explaining which angle does what "one last time".

I would like to thank Dr. Ruben Hühne and Sascha Trommler for their help with the RHEED system, and Dr. Konstantin Nenkov and Ulrike Besold for always being around in the SQUID room and the laser-lab.

A big thank you goes to my roommates, for constituting such a nice working environment; Orkidia Bilani (always "gute Laune"), Dr. Jong-Woo Kim (the coffee expert) and Andreas Herklotz ("There's been a fire in the PLD-chamber"), thank you for creative problem solving!